



HAL
open science

Satellite observations reveal a decreasing albedo trend of global urban cities over the past 35 years

Shengbiao Wu, Xingwen Lin, Zunjian Bian, Mathew Lipson, Raffaele Laforteza, Qiang Liu, Sue Grimmond, Erik Velasco, Andreas Christen, Valéry Masson, et al.

► **To cite this version:**

Shengbiao Wu, Xingwen Lin, Zunjian Bian, Mathew Lipson, Raffaele Laforteza, et al.. Satellite observations reveal a decreasing albedo trend of global urban cities over the past 35 years. *Remote Sensing of Environment*, 2024, 303 (9), pp.114003. <10.1016/j.rse.2024.114003>. <hal-04892192>

HAL Id: hal-04892192

<https://hal.science/hal-04892192v1>

Submitted on 16 Jan 2025

HAL is a multi-disciplinary open access archive for the deposit and dissemination of scientific research documents, whether they are published or not. The documents may come from teaching and research institutions in France or abroad, or from public or private research centers.

L'archive ouverte pluridisciplinaire **HAL**, est destinée au dépôt et à la diffusion de documents scientifiques de niveau recherche, publiés ou non, émanant des établissements d'enseignement et de recherche français ou étrangers, des laboratoires publics ou privés.



HAL Authorization

[Click here to view linked References](#)

1 **Title:** Satellite observations reveal a decreasing albedo trend of global urban cities over the past
2 35 years

3 **Author List:** Shengbiao Wu¹, Xingwen Lin², Zunjian Bian³, Mathew Lipson⁴, Raffaele
4 Laforzezza^{5,6}, Qiang Liu⁷, Sue Grimmond⁸, Erik Velasco⁹, Andreas Christen¹⁰, Valéry Masson¹¹,
5 Ben Crawford¹², Helen Claire Ward¹³, Nektarios Chrysoulakis¹⁴, Krzysztof Fortuniak¹⁵, Eberhard
6 Parlow¹⁶, Wlodzimierz Pawlak¹⁵, Nigel Tapper¹⁷, Jinkyu Hong¹⁸, Je-Woo Hong¹⁹, Matthias Roth²⁰,
7 Jiafu An²¹, Chen Lin²², Bin Chen^{1,23-24,*}

8 **Author Affiliation:**

9 (1) Division of Landscape Architecture, Faculty of Architecture, The University of Hong Kong,
10 Pokfulam, Hong Kong Special Administrative Region, China (shengwu@hku.hk)

11 (2) College of Geography and Environmental Sciences, Zhejiang Normal University, Jinhua
12 321004, China (linxw@zjnu.edu.cn)

13 (3) Stake Key Laboratory of Remote Sensing Science, Aerospace Information Research Institute,
14 Chinese Academy of Sciences, Beijing 100083, China (bianzj@aircas.ac.cn)

15 (4) Australian Research Council (ARC) Centre of Excellence for Climate System Science, Climate
16 Change Research Centre, Level 4, Mathews Building, UNSW Sydney, New South Wales, 2052,
17 Australia (m.lipson@unsw.edu.au)

18 (5) Department of Soil, Plant and Food Sciences (Di.S.S.P.A.), University of Bari Aldo Moro,
19 Via Amendola 165/A 70126 Bari, Italy (raffaele.laforzezza@uniba.it)

20 (6) Beijing Forestry University, Beijing 100083, China (raffaele.laforzezza@uniba.it)

21 (7) Pengcheng Laboratory, Shenzhen 518055, China (liuq03@pcl.ac.cn)

22 (8) Department of Meteorology, University of Reading, Reading, RG6 6ET, United Kingdom
23 (c.s.grimmond@reading.ac.uk)

24 (9) Molina Center for Energy and the Environment, Boston, USA (evelasco@mce2.org)

25 (10) Environmental Meteorology, Institute of Earth and Environmental Sciences, Faculty of
26 Environment and Natural Resources, University of Freiburg, Freiburg, Germany
27 (andreas.christen@meteo.uni-freiburg.de)

28 (11) Centre National de Recherches Météorologiques, University of Toulouse, Météo-France and
29 CNRS, Toulouse, France (valery.masson@meteo.fr)

30 (12) Geography and Environmental Sciences, University of Colorado, Denver, Colorado, USA
31 (benjamin.crawford@ucdenver.edu)

32 (13) Department of Atmospheric and Cryospheric Sciences, University of Innsbruck, Innsbruck,
33 Austria (Helen.Ward@uibk.ac.at)

34 (14) Foundation for Research and Technology Hellas, Institute of Applied and Computational
35 Mathematics, Remote Sensing Lab, Heraklion, Greece (zedd2@iacm.forth.gr)

-
- 36 (15) Department of Meteorology and Climatology, University of Lodz, Lodz, Poland
37 (krzysztof.fortuniak@geo.uni.lodz.pl; wlodzimierz.pawlak@geo.uni.lodz.pl)
38 (16) Department for Environmental Sciences, Meteorology, Climatology and Remote Sensing,
39 University Basel, CH-4056 Basel, Switzerland (eberhard.parlow@unibas.ch)
40 (17) School of Earth, Atmosphere and Environment, Monash University, Melbourne, Australia
41 (nigel.tapper@monash.edu)
42 (18) Ecosystem-Atmosphere Process Lab, Department of Atmospheric Sciences, Yonsei
43 University, Seoul, Republic of Korea (jhong@yonsei.ac.kr)
44 (19) Korea Environment Institute, Sejong, Republic of Korea (jwhong@kei.re.kr)
45 (20) Department of Geography, National University of Singapore, Singapore, Singapore
46 (geomr@nus.edu.sg)
47 (21) Department of Finance and Insurance, Faculty of Business, Lingnan University, Hong Kong
48 SAR, China (jiafuan@ln.edu.hk)
49 (22) Faculty of Business and Economics, The University of Hong Kong, Hong Kong SAR, China
50 (chenlin1@hku.hk)
51 (23) Urban Systems Institute, The University of Hong Kong, Hong Kong SAR, China
52 (binley.chen@hku.hk)
53 (24) HKU Musketeers Foundation Institute of Data Science, The University of Hong Kong, Hong
54 Kong SAR, China (binley.chen@hku.hk)

55
56

57 * **Corresponding Author:** Bin Chen (binley.chen@hku.hk)

58
59

60 Submission to *Remote Sensing of Environment*

61

62 **Figures/Tables Record:**

63 Number of figures/tables: 15 figures, 2 tables

64 Supporting materials: 20 figures, 2 table

65
66
67
68

69 **Abstract**

70 Urban surface albedo is an essential biophysical variable in the surface energy balance across all
71 scales, from micro-scale (materials) to global scale, changing with land cover and three-
72 dimensional (3-D) structure over urban areas. Urban albedos are dynamics over space and time
73 but have not yet been quantified over global scales due to the lack of high-resolution albedo
74 datasets. Here, we combined the direct estimation approach and Landsat surface reflectance
75 product to generate a 30-m-resolution annual surface albedo dataset for 3037 major cities (area >
76 50 km²) worldwide for the period from 1986 to 2020, allowing spatial patterns and long-term
77 temporal trends to be explored with possible causal drivers, and quantification of the surface
78 radiative forcing from these albedo changes. Evaluation of this new albedo dataset using global
79 urban flux tower-based measurements demonstrates its high accuracy with an overall bias and
80 root-mean-square-error (RMSE) of 0.005 and 0.025, respectively. Analysis of the dataset reveals
81 an overall trend of decreasing albedo for the 35-year evaluation period (1986-2020), which is
82 robust accounting for a series of uncertainties from training sample representativeness, Landsat
83 data uncertainty, seasonal variation, and snow-cover confounding impacts. Our results reveal that
84 urban greening (measured by the Normalized Difference Vegetation Index (NDVI) trend) can well
85 explain the total variances in the albedo trend for the 35-year period through two different
86 pathways of tree planting and urban warming-enhanced vegetation growth. The decrease in urban
87 albedo caused a warming effect indicated by positive surface radiative forcing, with a global city-
88 level average surface radiative forcing of 2.76 W·m⁻². These findings enhance our understanding
89 of urbanization's impacts on albedo-related biophysical processes and can provide information to
90 quantify urban surface radiation energy and design effective mitigation strategies to reduce urban
91 warming (e.g., urban heat islands).

92 **Keywords:** Biophysical process; NDVI; Radiative forcing; Landsat; MODIS; Surface albedo

93

94

95

96

98 **1. Introduction**

99 Urban areas represent the principal land cover that is most affected by intensive anthropogenic
100 activities from replacing agricultural, forested or natural landscapes with impervious surfaces
101 (Seto et al. 2012). Urbanization modifies the carbon exchange between the surface and atmosphere
102 (e.g., anthropogenic emissions of carbon dioxide (CO₂) from domestic heating, transport, industry
103 and services, and electricity generation; Ribeiro et al. 2019; Wang et al. 2015), as well as changes
104 surface radiative properties and energy partitioning (e.g., albedo and evapotranspiration; Cao et al.
105 2016; Schwaab et al. 2021), and thus modifies biophysical variables (e.g., air temperature). This
106 can result in nocturnal canopy air temperatures being warmer in urban areas than the surrounding
107 non-urban areas, known as the canopy layer urban heat island (CL-UHI) (Estoque et al. 2020; Oke,
108 1982). With a global urban population of 4.2 billion (around 55% of the total population in 2018)
109 projected to increase to 9.7 billion (about 68% of the total population) by 2050 (UNDESA, 2019),
110 the well-being of urban residents is at critical risk and simultaneously impact by urban-climate
111 phenomena, such as the CL-UHI (Huang et al. 2020; Hsu et al. 2021). Improving our
112 understanding of biophysical processes in cities can help to create more livable environments.

113

114 Surface albedo change can directly alter the biophysical processes of surface energy balance from
115 micro (materials) to local and to global scales. Urbanization causes albedo changes by modifying
116 surface materials and three-dimensional (3-D) structures (Shen et al. 2021). For example,
117 anthropogenic land cover changes between 1700 and 2005 are estimated to have caused a 0.00106
118 increase in global mean albedo, that is linked to a negative radiative forcing of $-0.15 \pm 0.10 \text{ W}\cdot\text{m}^{-2}$
119 (Ghimire et al. 2014; Myhre et al. 2014). For a long time, the use of highly reflective urban
120 materials (e.g., white rooftops and light-colored pavements) has been actively encouraged as
121 method to mitigate the surface-UHI (S-UHI) effect and improve human comfort (Morini et al.
122 2016; Rosso et al. 2018). Numerous regional and global climate simulations have shown albedo-
123 related impacts. A 0.1 increase in albedo in urban areas (e.g., rooftops and pavements) has been
124 estimated to be able to reduce the global average surface temperature by 0.01-0.07 K, which is
125 equivalent to a 25-150 billion ton offset in CO₂ emissions (Akbari et al. 2012; Menon et al. 2010;
126 Xu et al. 2020).

127
128 Urbanization impacts on surface albedo are multifaceted. Initial urbanization, changing a natural
129 vegetated surface (e.g., forest and grassland) to light colored short building may increase surface
130 albedo (Kuang et al. 2019), but the same materials with denser 3-D urban morphology will
131 generate more shadows, reducing the bulk surface albedo (Christen and Vogt, 2004; Groleau and
132 Mestayer, 2013). The net surface albedo change depends on both urban cover materials and
133 building arrangements (Falasca et al. 2019; Qin, 2015; Santamouris and Fiorito, 2021; Yang and
134 Li, 2015). Satellite remote sensing can quantify these net effects with global coverage. Coarse-
135 resolution satellites in previous studies based on the 500-m-resolution Moderate-Resolution
136 Imaging Spectroradiometer (MODIS) and Global LAnd Surface Satellite (GLASS) albedo
137 products were not able to accurately detect the fine-scale heterogeneity of urban albedo
138 (Chrysoulakis et al. 2018; Hu et al. 2016; Tang et al. 2018). Use of higher-resolution satellite
139 observations (e.g., 30-m Landsat and 10-m Sentinel-2) demonstrated their potential to monitor
140 fine-scale urban albedo (Bonafoni and Sekertekin, 2020; Guo et al. 2022; Trlica et al. 2017).

141
142 However, our spatiotemporal knowledge of urban albedo is limited for several reasons. First,
143 existing satellite-based albedo studies are restricted to very few (≤ 11) cities (Guo et al. 2022;
144 Trlica et al. 2017), so the spatiotemporal trends may be city-specific. Second, the underlying
145 drivers controlling the spatiotemporal patterns of surface albedo and their resulting climatic effects
146 remain largely unclear. Urbanization are complex physical, socioeconomic, and cultural processes
147 in 3-D space, involving extent expansion of new impervious areas (Liu et al. 2020; Zhang and Seto,
148 2011) and increase in human modification on mature urban areas, such as building construction
149 and greening activity (Theobald et al. 2020; Zhou et al. 2022). Previous studies attributed urban
150 albedo variations to land cover change from natural lands to new urban structure by making the
151 use of two-baseline-year datasets, without accounting for human modification activities (Ouyang
152 et al. 2022). For example, large-scale tree planting in cities is a global agreement and effort to
153 mitigate urban heat stress from climate warming and CL-UHI effects (Schwaab et al. 2021).
154 Around 70% of cities worldwide witness urban greening phenomenon with increasing vegetation
155 coverage (Sun et al. 2020; Zhang et al. 2021) and enhanced vegetation growth due to CO₂
156 fertilization and longer growing seasons (Hwang et al. 2022; Meng et al. 2020; Wang et al. 2019).

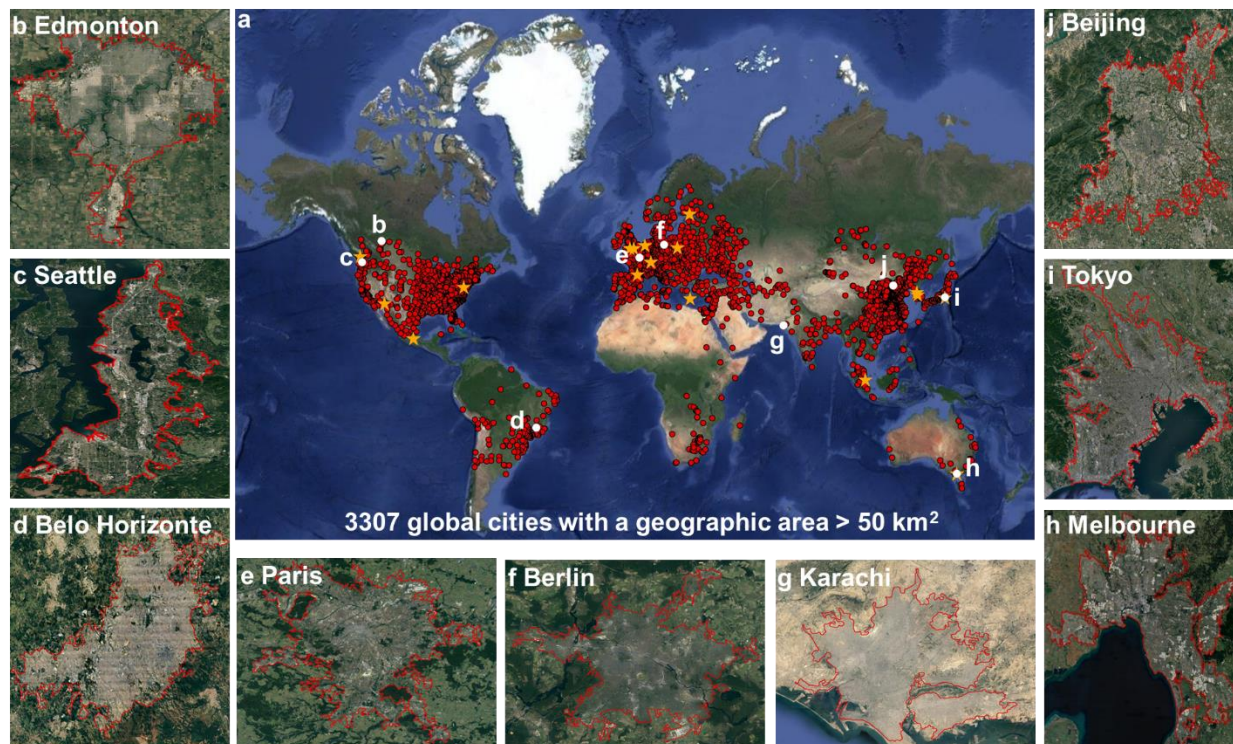
157 These actions have substantially reshaped urban landscapes, but to what extent urban greening
158 impacts the change of surface albedo and albedo-related climatic effects remains unknown.

159
160 In such a context, the main objective of this study is to explore the spatiotemporal characteristics
161 of albedo in cities globally and to decipher the underlying drivers of albedo change. By applying
162 our previously developed direct estimation approach on the Google Earth Engine (GEE) cloud-
163 computing platform, we construct an annual mean albedo dataset covering 35 years (1986-2020)
164 for 3037 major global cities. Based on the novel dataset, we analyze the spatial and temporal
165 patterns of urban albedo and assess the causes of albedo change linked to vegetation greening
166 observed in Landsat-derived normalized difference vegetation index (NDVI) data. Lastly, we
167 quantify the albedo-induced surface radiative forcing to model climatic responses from urban
168 surface albedo change.

169
170 **2. Study area and materials**

171 **2.1. City areas**
172 The city areas were extracted from the 2018 Global Urban Boundary (GUB) product, which is
173 based on 30-m-resolution global artificial impervious area product (GAIA; Li et al. 2020), using
174 two criteria (Chen et al. 2022): (1) a spatial extent larger than 50 km²; and (2) availability of at
175 least 30-year valid Landsat observations during the 35 evaluated years (1986-2020). A total of
176 3037 urban areas globally (hereafter referred to as cities) satisfied these criteria and were selected
177 (**Fig. 1**). Almost all cities have over 20 available Landsat images for each one-year cycle, with the
178 annual average observation number ranging from 21 to 40 and a mean value of 30, indicating the
179 capability to capture inter- and intra-year variations of urban surface albedo (**Figs. S1 and S2**).

180



181
 182 **Fig. 1.** Urban areas (cities) used in this study. **(a)** City location globally (red dots), urban flux
 183 towers (yellow pentagrams), and example of nine cities with boundaries (red polygons) as defined
 184 by the Global Urban Boundary (GUB) product in 2018: **(b)** Edmonton, **(c)** Seattle, **(d)** Belo
 185 Horizonte, **(e)** Paris, **(f)** Berlin, **(g)** Karachi, **(h)** Melbourne, **(i)** Tokyo, and **(j)** Beijing. The 3037
 186 global cities are selected with an area extent larger than 50 km². 21 worldwide urban flux tower
 187 sites come from two collaborative projects: 19 flux sites from the Urban-PLUMBER multi-site
 188 model evaluation project (Lipson et al. 2022a, 2022b) and 2 flux sites from the URBANFLUXES
 189 project (Chrysoulakis et al. 2018; Feigenwinter et al. 2018). Background and city pictures are
 190 extracted from the Basemap of Google Earth (Google. Inc).

191
 192 **2.2. Datasets**

193 Five multi-source datasets are used in this study for different purposes: (1) surface reflectance data
 194 (i.e., Landsat-5, Landsat-7, and Landsat-8 surface reflectance products; Gorelick et al. 2017); (2)
 195 surface Bidirectional Reflectance Distribution Function (BRDF) data (i.e., MCD43A1; Wang et
 196 al. 2018); (3) surface albedo data, (i.e., flux tower-based measurements and MCD43A3;
 197 Feigenwinter et al. 2018; Lipson et al. 2022a, 2022b; Wang et al. 2018); (4) land cover type data
 198 (i.e., European Space Agency (ESA) WorldCover and MCD12Q1; Sulla-Menashe et al. 2018;
 199 Zanaga et al. 2021); and (5) downward solar radiation data, (i.e., the Bias-adjusted RAdiation
 200 Dataset (BaRAD) product; Chakraborty and Lee, 2021). **Table 1** summarizes the ancillary
 201 information of these datasets, including data category, dataset name, spatial coverage, ground

202 resolution, observation period, usage description, and related references. **Table 2** provides detailed
203 information for the 21 urban flux towers used for albedo validation.

204

205 **2.2.1. Landsat surface reflectance product**

206 We used 35-years (1986-2020) of the Landsat Level-2 surface reflectance (Collection 2, Tier 1)
207 product with a 30-m spatial resolution derived from three Landsat satellites (i.e., Landsat-5 TM,
208 Landsat-7 ETM+, and Landsat-8 OLI; Gorelick et al. 2017, **Table 1**). Landsat provides the longest
209 high-quality global surface reflectance record available (Wulder et al. 2022). Landsat-5 TM and
210 Landsat-7 ETM+ sensors have six spectral bands spanning three visible (i.e., blue, green, and red),
211 one near-infrared (NIR), and two shortwave infrared (SWIR) bands, whereas Landsat-8 OLI has
212 one additional ultra-blue spectral band. The pixel-level quality assurance (QA) auxiliary data for
213 each surface reflectance dataset gives a bitmask metric indicating cloud, cloud shadow, snow, and
214 ice conditions. To minimize the uncertainty caused by the Landsat-7 scan line off failure on albedo
215 estimation (Qiu et al. 2021; Zhang and Roy, 2016), we primarily focused on the use of Landsat-5
216 and Landsat-8 satellite data, with data availabilities of 26-year (1986-2011) Landsat-5 TM, 2-year
217 (2012-2013) Landsat-7 ETM+, and 7-year (2014-2020) Landsat-8 OLI.

218

219 **2.2.2. MODIS BRDF/albedo product**

220 We used the 500-m spatial resolution MODIS BRDF product (MCD43A1, Collection 6; **Table 1**)
221 in 2000-2020 to provide a high-quality surface BRDF/albedo training library (Wang et al. 2018).
222 MCD41A1 is the most accurate satellite BRDF/albedo product and has been widely used for the
223 training and calibration of the direct estimation approaches (Guo et al. 2022; Qu et al. 2013). In
224 addition, the MCD43A3 albedo product was used for the spatiotemporal analysis of urban surface
225 albedo for comparisons with Landsat albedo. MCD43A3 is derived from MCD43A1 and provides
226 black-sky albedo (BSA) and white-sky albedo (WSA) data at local solar noon for MODIS seven
227 spectral bands and three broadbands (i.e., visible, NIR, and shortwave).

228

229 **2.2.3. Land cover type products**

230 Two land cover type products are used (**Table 1**): 10-m ESA WorldCover for 2020, and 500-m
231 MCD12Q1 products (Collection 6) from 2001 to 2020, for selecting training samples. WorldCover
232 is generated from Sentinel-1 and Sentinel-2 data, with a similar algorithm framework for the

233 annual Copernicus Global Land Service Land Cover (CGLS-LC) product (Buchhorn et al., 2020).
234 This dataset provides 11 land cover classes (i.e., tree cover, shrubland, grassland, cropland, built-
235 up, bare/sparse vegetation, snow and ice, open water, herbaceous wetland, mangroves, and moss
236 and lichen) with an overall global accuracy of 74.4% (Zanaga et al. 2020). It is freely accessible
237 to the academic community (Zanaga et al. 2020). MCD12Q1 is generated by a supervised
238 classification approach from MODIS reflectance with five legacy classification schemes (Sulla-
239 Menashe and Friedl, 2018). We selected the International Geosphere-Biosphere Programme
240 (IGBP) classification scheme for data analysis. The “built-up” definitions in these two land cover
241 products have a slight difference. For WorldCover, “built-up” is defined as land covered by
242 buildings, roads and other man-made structures, which excludes urban green areas (Zanaga et al.
243 2020). For MCD12Q1, “urban and built-up lands” is defined as surface covered by at least 30%
244 of impervious area, such as building materials, asphalt, and vehicles (Sulla-Menashe and Friedl,
245 2018).

246

247 **2.2.4. Surface downward solar radiation data**

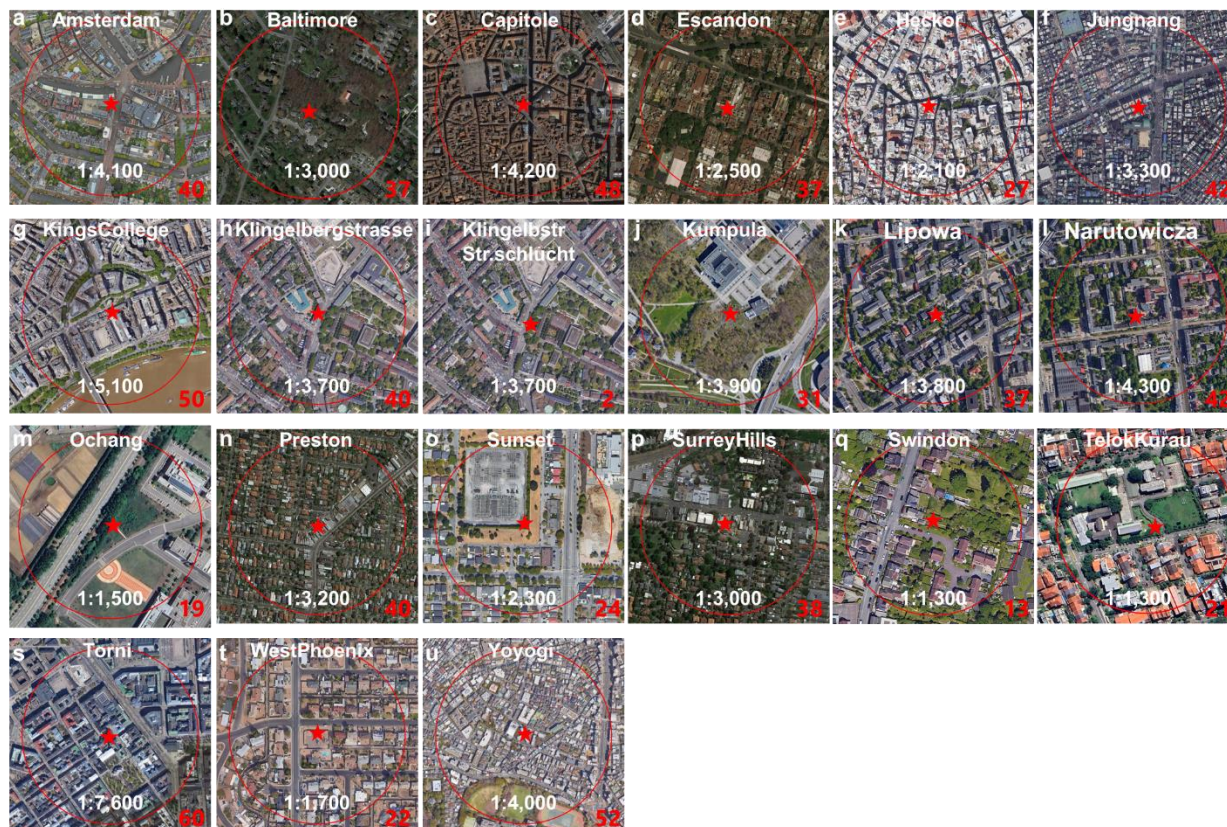
248 We used the 40-year (1980-2019) $0.5^\circ \times 0.625^\circ$ monthly BaRAD solar radiation dataset (**Table 1**)
249 owing to its temporal window overlapping with Landsat. BaRAD is generated from the Modern-
250 Era Retrospective analysis for Research and Applications, version 2 (MERRA-2) global reanalysis
251 dataset using a bias-correction random forest algorithm, trained with Global Energy Balance
252 Archive (GEBA) observations from 2500 worldwide ground stations (Wild et al. 2017). BaRAD
253 is bias-adjusted (cf. MERRA-2) thus has high accuracy (Chakraborty and Lee, 2021). BaRAD
254 provides three radiation components: total incoming shortwave, incoming direct beam, and
255 incoming diffuse radiation. BaRAD data are used here to determine: (1) the fraction of diffuse
256 radiation relative to the total incoming shortwave radiation, for the blue-sky albedo calculation
257 (**Section 3.1**); and (2) the surface radiative forcing induced by albedo changes (**Section 3.5**).

258

259 **2.2.5. Tower-based radiation flux measurements**

260 To evaluate the accuracy of our algorithm, we used downward and upward solar radiation
261 measurements from 21 urban flux towers located throughout the world, including cities in Asia,
262 Australia, Europe, and North America (**Fig. 1a**). The data collected by these towers were put
263 together as part of two collaborative projects: Urban-PLUMBER (19 sites; Lipson et al. 2022a,

264 2022b) and URBANFLUXES (2 sites; Chrysoulakis et al. 2018; Feigenwinter et al. 2018). The
 265 sensors on these towers are mounted at heights ranging from 2 to 60 meters above the ground, with
 266 viewing footprints where impervious surfaces (i.e., buildings, roads, paved areas) cover between
 267 31% and 97% of the plan area (**Fig. 2; Table 2**). The radiation flux measurements are used as
 268 ground truths for assessing the accuracy of surface albedo estimates derived from Landsat satellites.



269
 270 **Fig. 2.** Google Earth satellite images of flux sites (red pentagrams) and the associated radiation
 271 footprint areas (red circles) for (a) Amsterdam, (b) Baltimore, (c) Capitole, (d) Escandon, (e)
 272 Heckor, (f) Jungnang, (g) KingsCollege, (h) Klingelbergstrasse, (i) KlingelbstrStr.schlucht, (j)
 273 Kumpula, (k) Lipowa, (l) Narutowicza, (m) Ochang, (n) Preston, (o) Sunset, (p) SurreyHills, (q)
 274 Swindon, (r) TelokKurau, (s) Torni, (t) WestPhoenix, and (u) Yoyogi. The map scales and tower
 275 heights (in meters) are shown at the bottom of each image in white and red, respectively. Note:
 276 Footprint area (with a 25-m diameter) of the KlingelbstrStr.schlucht site in panel (i) is overlapped
 277 by red pentagram symbol.

278
 279 **3. Methods**

280 **3.1. Estimation of annual urban surface albedo from Landsat**

281 We adopted our recently developed direct estimation approach to retrieve surface albedo from
 282 Landsat satellites (Lin et al. 2022), with three key steps summarized as follows (**Fig. 3**):

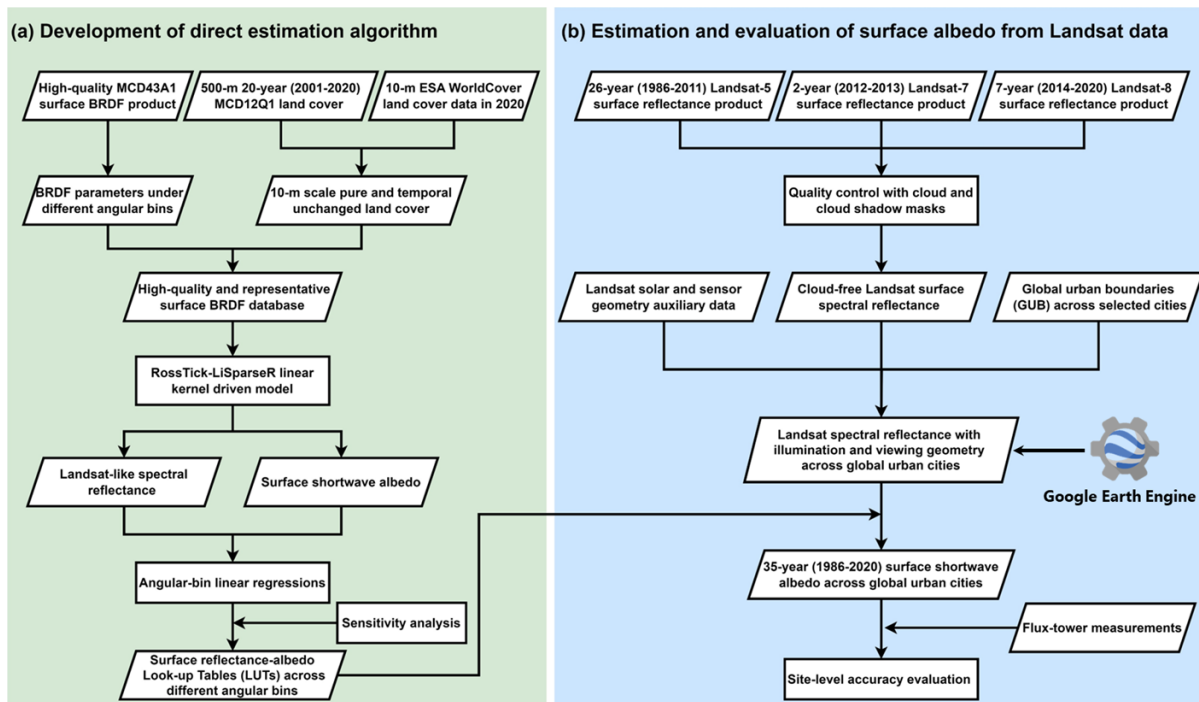
283
284 **(1) Selection of high-quality surface BRDF/albedo datasets.** High-quality BRDF/albedo
285 training datasets are the key to the direct estimation approach. To this end, we used the MCD43A1
286 BRDF/albedo product with ESA WorldCover and MCD12Q1 land covers to screen the
287 BRDF/albedo library that is representative at 30-m scale (Lin et al. 2022) with four criteria: (i)
288 high assurance with the pixel-level QA of 0; (ii) homogeneous coverage (with the pixel-level land
289 cover purity $\geq 95\%$ indicated by the 10-m ESA WorldCover data); (iii) diverse land cover
290 (including 16 dominant land types following the IGBP classification scheme); and (iv) reasonable
291 data range (that refers to the pairs of reflectance and albedo within a physical range of 0-1). We
292 considered this surface BRDF/albedo dataset from mixed land covers as a general scheme and
293 compared it with the BRDF/albedo dataset from pure urban land cover (referred to as urban scheme)
294 in the sensitivity analysis of algorithm development (**Section 5.1.1**), which shows a consistent
295 performance.

296
297 **(2) Generation of training and testing datasets.** Based on the selected BRDF/albedo library, we
298 simulated Landsat-like surface reflectance in two steps. First, we simulated MODIS-like surface
299 reflectance across its seven spectral bands using the linear RossThick-LiSparseR BRDF model
300 (Lucht et al. 2000) with optimized angular settings (i.e., a 2° interval for solar zenith, viewing
301 zenith, and local solar zenith angles; and a 5° interval for relative azimuth angle). Second, we
302 converted the MODIS-like surface reflectance to the Landsat-like surface reflectance using band
303 conversion coefficients derived using similar approaches to Qu et al. (2013). Considering the
304 different spectral configurations for Landsat satellites (**Table S1**), we simulated surface reflectance
305 datasets across six spectral bands for Landsat-5 TM and Landsat-7 ETM+, and across seven
306 spectral bands for Landsat-8 OLI. We also simulated surface shortwave albedo from the MODIS
307 BRDF/albedo library in two steps. First, we simulated spectral BSA and WSA datasets under clear-
308 sky and perfectly diffuse illumination conditions, respectively. Second, we converted the spectral
309 BSA and WSA albedo datasets to shortwave albedo using the regression coefficients proposed by
310 Liang et al. (2002).

311
312 **(3) Build-up of reflectance-to-albedo look-up-tables (LUTs).** With the pairs of simulated

313 Landsat-like surface reflectance and surface shortwave albedo, we created LUTs of reflectance-
 314 to-albedo relations using the linear regression approach for each angular setting (He et al. 2018;
 315 Qu et al. 2013). To minimize the potential impact from Landsat satellite orbital drifts (e.g.,
 316 Landsat-5 drifted between 1995-2000 and 2003-2007, Landsat-7 drifted from 2017 to the present;
 317 Qiu et al. 2021; Zhang and Roy, 2016), we trained spectral reflectance and shortwave albedo
 318 relations for local solar noon (e.g., 12:00 p.m.) geometry that is independent from instantaneous
 319 satellite observation time.

320



321

322 **Fig. 3.** Satellite-based direct estimation of surface albedo from Landsat, with two major steps: **(a)**
 323 direct estimation algorithm development, and **(b)** surface albedo estimation and evaluation.

324

325 We applied our reflectance-to-albedo LUTs (BSA and WSA; Eq. 1) on the Google Earth Engine
 326 (GEE, Gorelick et al. 2017) cloud-computing platform to estimate urban surface albedo for global
 327 cities using four steps. First, we used the pixel-level QA auxiliary layer to exclude cloud, cloud
 328 shadow, and snow contaminated pixels in Landsat surface reflectance. Second, we estimated BSA
 329 and WSA from the quality-controlled Landsat surface, where the solar geometry is extracted from
 330 metadata and sensor geometry is set as nadir due to small variations in Landsat sensor viewing ($<$
 331 7.5° ; Nagol et al. 2015). Third, we calculated annual blue-sky albedo from BSA and WSA by using
 332 the diffuse fraction (i.e., fraction of diffuse radiation in total illumination radiation) from the

333 BaRAD dataset. Based on Landsat spectral reflectance, we also calculated the annual NDVI as an
 334 indicator of vegetation cover. Finally, we stored Landsat-derived blue-sky albedo and NDVI as
 335 two separate data layers for each city over 35 years. To verify the feasibility of the direct estimation
 336 approach with training samples from mixed land covers over urban areas, we also compared the
 337 algorithm with the training samples of pure urban cover in the discussion section.

$$338 \alpha = C_0(\theta_s, \theta_v, \varphi) + \sum_{i=1}^N C_i(\theta_s, \theta_v, \varphi) \times \rho_L(\lambda_i) \quad (1)$$

339 where α is the surface shortwave albedo (BSA and WSA); $\rho_L(\lambda_i)$ is the Landsat surface reflectance
 340 at spectral band λ_i ($i = 1, 2, 3, \dots, N$; $N = 6, 6,$ and 7 for Landsat-5, Landsat-7, and Landsat-8,
 341 respectively); and $C_i(\theta_s, \theta_v, \varphi)$ denotes the regression coefficient at spectral band λ_i for solar zenith
 342 angle θ_s , view zenith angle θ_v , and relative azimuth angle φ .

343

344 **3.2. Evaluation of urban albedo with radiation data from urban flux towers**

345 We evaluated the accuracy and uncertainty of Landsat blue-sky albedo using observed albedo
 346 calculated from the incoming and outgoing shortwave radiation measured by 21 urban sites (**Table**
 347 **2**). To match the Landsat-derived albedo at local solar noon and minimize diurnal variations
 348 (Minnis et al. 1997), we used observations from 11:00 a.m. to 1:00 p.m. local standard time. As
 349 the diffuse fraction (d) is not recorded by these flux tower datasets and the BaRAD dataset is too
 350 coarse for site-scale albedo calculation, we thus adopted a two-step strategy: (1) if the MODIS
 351 Aerosol product (MOD08) has high-quality Aerosol Optical Depth (AOD) observation over the
 352 target flux site, the radiative transfer simulation approach was applied (Wang et al. 2018); and (ii)
 353 otherwise, we adopted an empirical approach shown in Eq. 2 to calculate diffuse fraction d (Stokes
 354 and Schwartz, 1994):

355

$$356 d = 0.122 + 0.85 \times \exp(-4.8 \times \cos(\theta_s)) \quad (2)$$

357

358 We used the radiation flux footprint estimated from sensor height (**Table 2**; Román et al. 2009) to
 359 crop the pixel-level Landsat blue-sky albedo image and calculate the corresponding albedo average,
 360 and then compared this Landsat blue-sky albedo average with the tower-based albedo measured
 361 on the same dates. For the accuracy assessment, four commonly used metrics were used: bias
 362 (mean difference between Landsat-derived and tower-based albedo), root-mean-square-error
 363 (RMSE), relative root-mean-square-error (rRMSE, the ratio between RMSE and the measured

364 albedo mean), and coefficient of determination (R^2), with equations as follows:

365

366
$$Bias = \frac{1}{N} \sum_{i=1}^N (\alpha_{Landsat,i} - \alpha_{ground,i}) \quad (3)$$

367
$$RMSE = \sqrt{\frac{1}{N} \sum_{i=1}^N (\alpha_{Landsat,i} - \alpha_{ground,i})^2} \quad (4)$$

368
$$rRMSE = \frac{RMSE}{\overline{\alpha_{ground}}} \times 100\% \quad (5)$$

369
$$R^2 = \frac{\sum_{i=1}^N (\alpha_{Landsat,i} - \overline{\alpha_{Landsat}})(\alpha_{ground,i} - \overline{\alpha_{ground}})}{\sum_{i=1}^N (\alpha_{Landsat,i} - \overline{\alpha_{Landsat}})^2 \sum_{i=1}^N (\alpha_{ground,i} - \overline{\alpha_{ground}})^2} \quad (6)$$

370

371 where $\alpha_{Landsat,i}$ and $\alpha_{ground,i}$ are *i*th Landsat-derived and ground-measured albedo; $\overline{\alpha_{Landsat}}$ and
372 $\overline{\alpha_{ground}}$ are the average values of Landsat-derived and ground-measured albedo; N is the number
373 of observations.

374

375 **3.3. Spatiotemporal characteristic analysis of surface albedo in global cities**

376 We calculated the 35-year city-scale blue-sky albedo mean from Landsat albedo time series to
377 explore its spatial patterns. To further examine the temporal trends, we used the non-parametric
378 Mann-Kendall statistic (Mann, 1945) and the non-parametric Theil–Sen slope estimator (Theil,
379 1950) approaches, which do not require specific data distribution and are robust to outliers (Wang
380 et al. 2019), to calculate the magnitude and direction of the pixel-level monotonic albedo trend at
381 a statistical significance level of 0.05 (i.e., p -value < 0.05). The city-scale albedo trend is calculated
382 as the aggregation mean of all pixels that passed the significance test within the city area. The
383 spatiotemporal patterns of Landsat blue-sky albedo are undertaken for two periods (1986-2020
384 and 2001-2020). For comparison, we extracted 35-year city-scale spatiotemporal patterns of
385 MODIS blue-sky albedo in 2001-2020, which is calculated from the integration of MODIS BSA,
386 WSA, and BaRAD-derived diffuse fraction.

387

388 **3.4. Associations between urban greening and albedo change**

389 We explored the multifaceted associations between urban greening and albedo change in several
390 steps. First, the spatiotemporal patterns of Landsat NDVI in the 1986-2020 and 2001-2020 time

391 periods were calculated and aggregated to city-level means. Second, the intra- and inter-city
392 associations between urban albedo and NDVI trends were analyzed. Local examples in four typical
393 cities: two rapid-urbanized Shenzhen city (22° 32' 29.4" N, 114° 3' 34.56" E), China and
394 Birmingham city (52° 29' 10.47"N, 1° 53' 25.44"W), United Kingdom, together with two well-
395 urbanized Milton city (30°37'49.0"N 87°02'47.0"W), Florida, and Pinehurst city (36° 41' 43" N,
396 119° 0' 57" W), North Carolina, United States, were selected to showcase different pathways by
397 which urban greening modulates surface albedo during the urbanization process. Lastly, the
398 associations between urban albedo and vegetation in 2-D (measured by NDVI) and 3-D (measured
399 by vegetation height from 10-m-resolution Sentinel-2; Lang et al. 2023) were investigated to
400 elucidate the effects of urban greenery on surface albedo using data at the baseline year 2020.

401

402 **3.5. Urban surface radiative forcing induced by albedo change**

403 Changes in radiative forcing can be caused by natural and/or anthropogenic drivers (Shindell et al.
404 2013). A positive radiative forcing occurs when there is more incoming than outgoing energy (i.e.,
405 warming), whereas a negative radiative forcing (outgoing > incoming energy) results in a cooling
406 effect. We quantified the urban surface radiative forcing (*RF*) from albedo changes (Chen et al.
407 2015) using the following equation:

408

$$409 \quad RF = -K_{\downarrow} \times (\alpha_{t2} - \alpha_{t1}) \quad (7)$$

410

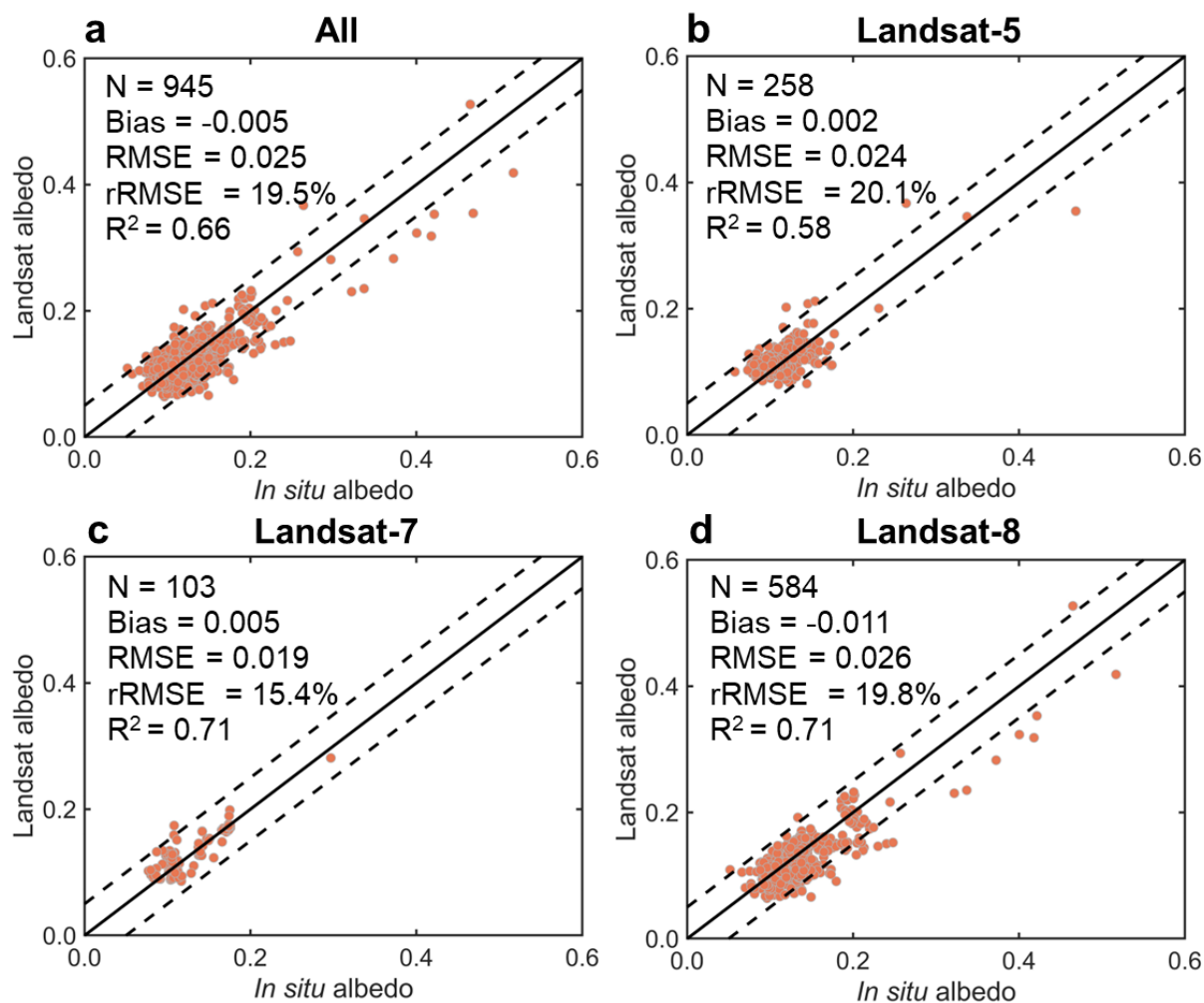
411 where K_{\downarrow} is the mean incoming or downward shortwave solar radiation between years t_1 and year
412 t_2 ; and $\alpha_{t2} - \alpha_{t1}$ is the surface albedo difference between those years. We used BaRAD and Landsat-
413 derived blue-sky albedo to derive pixel-scale RF (Eq. 7) and then calculated the city-scale RF from
414 pixel-scale data. To minimize the impact of fluctuations in annual albedo, we used a 5-year average
415 annual albedo for the RF calculation in 1986-2020. Namely, the mean surface albedo (α_{t1}) was
416 estimated for the 1986-1990 period, and α_{t2} for the 2016-2020 period, and K_{\downarrow} was estimated as the
417 mean downward shortwave solar radiation between 1991 and 2015.

418

419 **4. Results**

420 **4.1. Accuracy assessment of Landsat urban albedo**

421 We assessed the accuracy of Landsat-derived surface albedo using the flux tower-based
 422 observations (**Table 2**). Across the 21 flux tower sites, Landsat satellites individually achieve a
 423 high albedo accuracy (bias = -0.011 - 0.005, RMSE = 0.019 - 0.026, rRMSE = 15.4% - 20.1%, R^2
 424 = 0.58 - 0.71; **Fig. 4b-d**). For all three Landsat satellites, the overall accuracy is also reliable (bias
 425 = 0.005, RMSE = 0.025, rRMSE = 19.5%, $R^2 = 0.66$; **Fig. 4a**). Temporal validation for individual
 426 (**Fig. S3**) and combined (**Fig. S4**) years show similar accuracy patterns. These assessment results
 427 suggest that the Landsat-derived albedo dataset is reliable and can be used to analyze the
 428 spatiotemporal characteristics of surface albedo of cities globally.



429
 430 **Fig. 4.** Evaluation of Landsat-derived albedo with flux-tower measurements for (a) all three
 431 Landsat satellites, (b) Landsat-5, (c) Landsat-7, and (d) Landsat-8. The following comparison
 432 statistics are calculated: N (number of Landsat data observed on the same date as flux-tower
 433 measurements), bias (mean difference between Landsat-derived and tower-based albedo), RMSE
 434 (root-mean-square-error), rRMSE (relative RMSE, ratio between RMSE and measured albedo
 435 mean) and R^2 (coefficient of determination), 1:1 line (solid line), error lines of -0.05 and 0.05

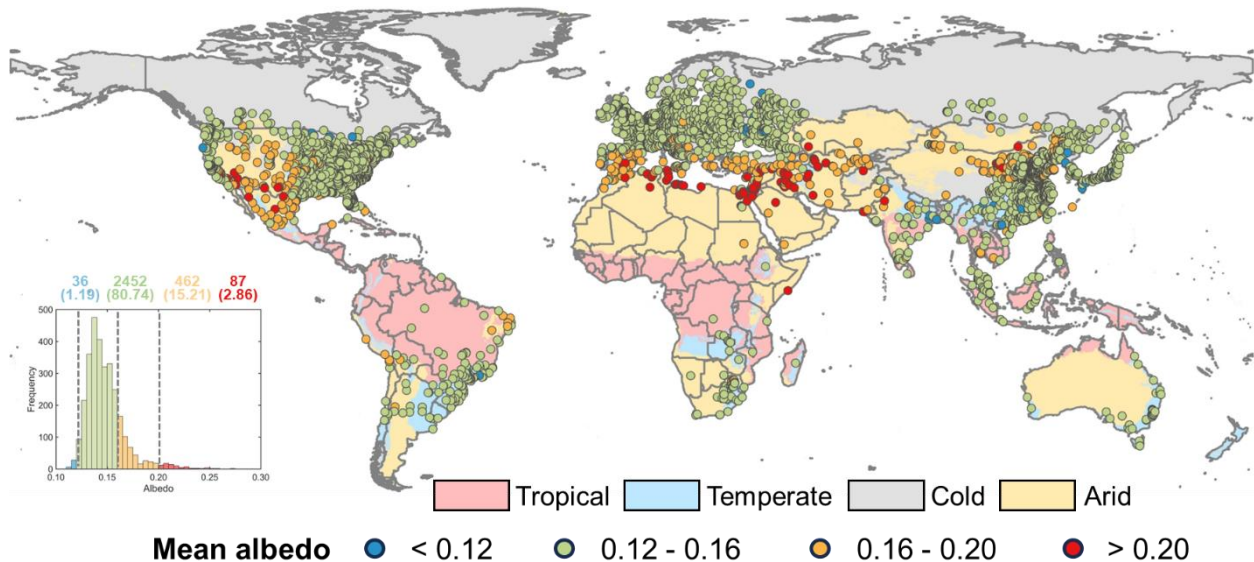
436 (dashed line).

437

438 4.2. Global variations of urban albedo

439 The 35-year (1986-2020), city-wide mean surface albedos for the 3037 global cities assessed here
440 have clear spatial patterns (**Fig. 5**). Cities in temperate climates have the lowest mean albedo (0.143,
441 N = 1340), followed by those in cold (0.144, N = 1073), tropical (0.145, N = 161), and arid (0.174,
442 N= 463) regions. Cloud cover limits the number of tropical cities meeting the threshold of having
443 35-year data. The albedo range for tropical cities (0.115-0.240) is in line with the range reported
444 by Rechid et al (2009) (0.10-0.20). The urban albedo distribution is skewed, with most cities (2452)
445 within the range of 0.12-0.16, followed by 462 cities within the range of 0.16-0.20, 87 cities with
446 albedos > 0.2, and only 36 cities < 0.12. The 20-year (2001-2020) city-level annual mean albedo
447 from the MODIS and Landsat datasets are close to those of the 35-year Landsat equivalence (**Fig.**
448 **S5**), with the majority of cities within the range of 0.12-0.20 and very few presenting albedos <0.12
449 or > 0.20.

450



451

452 **Fig. 5.** City-level average annual albedo (lower key) derived from 35-year (1986-2020) Landsat
453 data for 3037 global cities mapped onto 1-km Köppen-Geiger climate (Beck et al. 2018) (upper
454 key), with the number of cities (and the associated percentage in parentheses) given above the
455 inserted histogram.

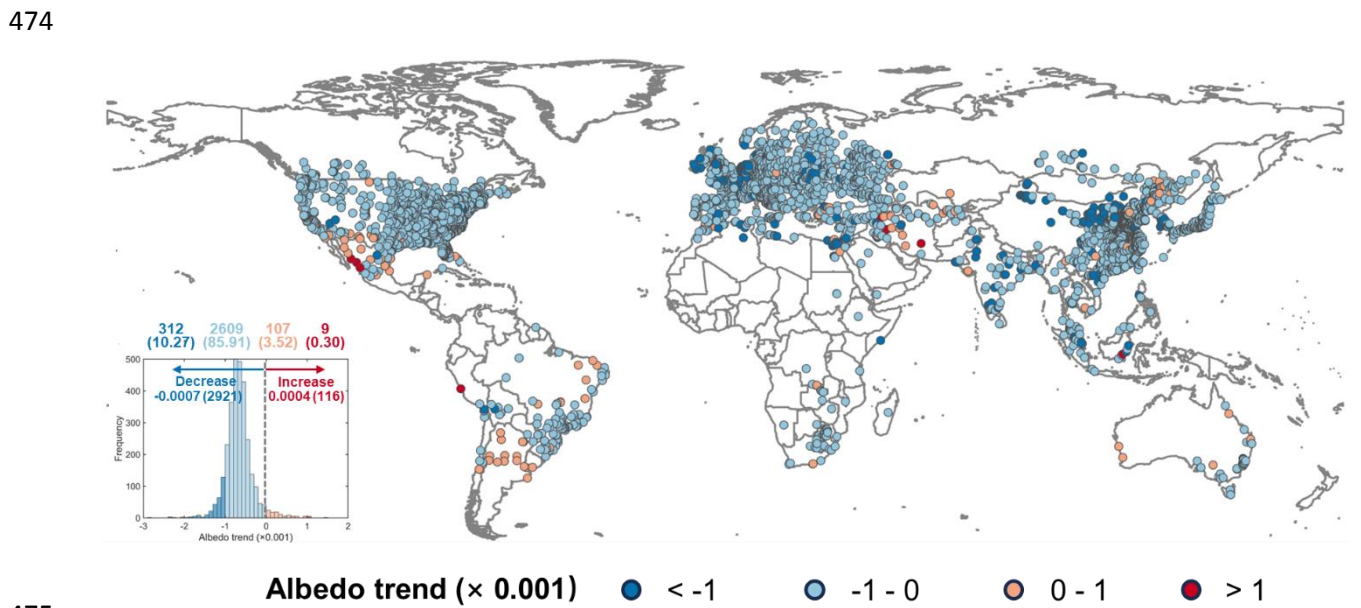
456

457 4.3. Global variations of urban albedo trend and driver attribution

458 4.3.1. Global temporal trends of urban albedo

459 The 35-year (1986-2020) trend of city-scale annual mean surface albedo depicts a negative slope
 460 of -0.0007 yr^{-1} (**Fig. 6**). When cities are subdivided by their mean trend, 2921 shows a decreasing
 461 trend (mean trend = -0.0007 yr^{-1}) and 116 an increasing trend (mean trend = 0.0004 yr^{-1}). Rapid
 462 changes, lower than -0.001 yr^{-1} , were observed in 312 cities across Europe, North America, East
 463 Asia, and the Middle East. Most cities are in the $-0.001 - 0.000 \text{ yr}^{-1}$ (2609) and 0.000 to 0.001 yr^{-1}
 464 $^{-1}$ (107) albedo change rate. Nine cities with a larger increasing albedo trend ($> 0.001 \text{ yr}^{-1}$) were
 465 observed in the Southwest region of the United States.

466
 467 The 21-year (2000-2020) trends for MODIS and Landsat consistently decrease (**Figs. S6**), at rates
 468 of -0.0003 yr^{-1} and -0.0014 yr^{-1} , respectively. Due to its inability to detect fine-scale urban
 469 heterogeneity, the 500-m-resolution MODIS satellite returns a lower decreasing rate than the 30-
 470 m-resolution Landsat (**Fig. S7**), supporting the necessity of using high-resolution satellite data to
 471 monitor urban environments. The 21-year change rate (-0.0014 yr^{-1}) is twice as high as the 35-year
 472 trend (-0.0007 yr^{-1}) for Landsat, indicating that the rate of worldwide urban albedo decrease has
 473 grown.

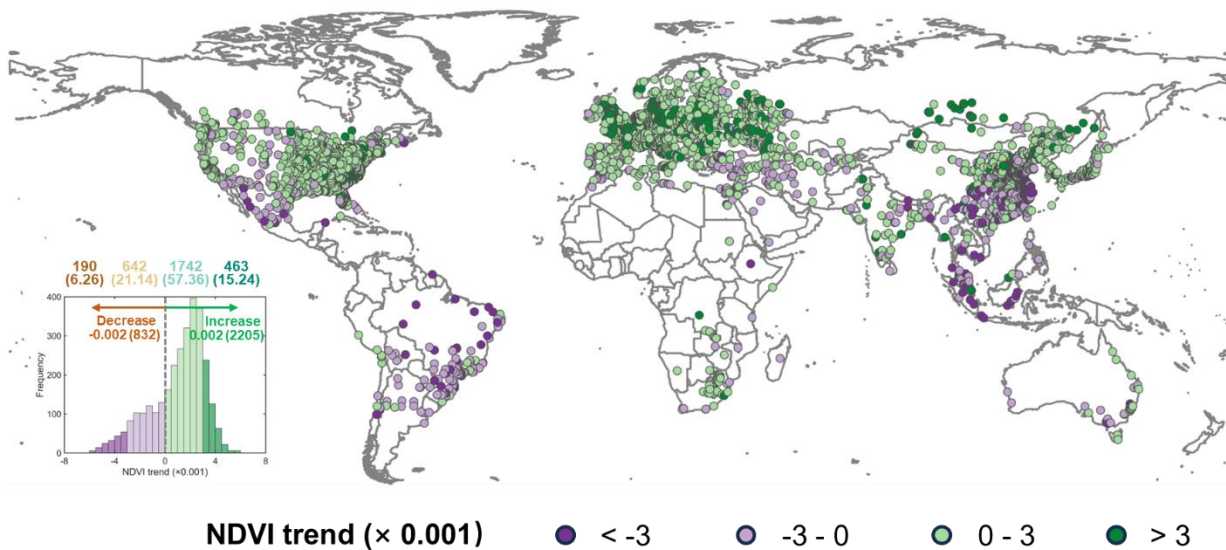


476 **Fig. 6.** Spatial patterns of the Landsat-derived city-level albedo trend for 3037 global cities over
 477 35 years (1986-2020), with the albedo trend histogram and the number of cities (with the related
 478 percentage in parentheses) given above the inserted histogram.

479
 480 **4.3.2. Associations between urban albedo and greenness**

481 Greening activity is one potential driver influencing urban albedo change. Landsat NDVI has a
 482 mean increase of 0.001 yr^{-1} for these 3037 cities during the same 35-year period, with 2205 cities
 483 exhibiting an increase (i.e., greening) and 832 experiencing a decrease (i.e., browning, **Fig. 7**).
 484 Most cities are in the 0.000 to 0.003 yr^{-1} (1742) and -0.003 to 0.000 yr^{-1} (642) NDVI change range,
 485 followed by 463 cities with an increasing NDVI trend $> 0.003 \text{ yr}^{-1}$ and 190 cities with a decreasing
 486 NDVI trend $< -0.003 \text{ yr}^{-1}$. Browning cities are predominantly found in East Asia, South America,
 487 and the Southwest region of the United States.

488



489

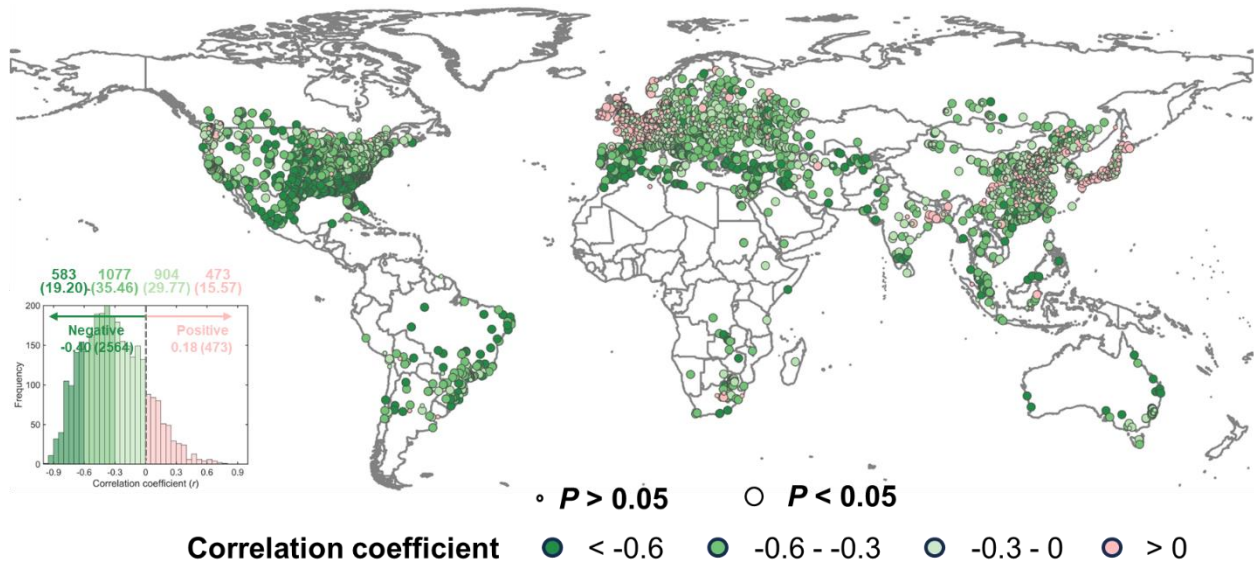
490 **Fig. 7.** Spatial patterns of the Landsat-derived city-level normalized difference vegetation index
 491 (NDVI) trend for 3037 global cities over 35 years (1986-2020), with the NDVI trend histogram
 492 and the number of cities (with the related percentage in parentheses) given above the inserted
 493 histogram.

494

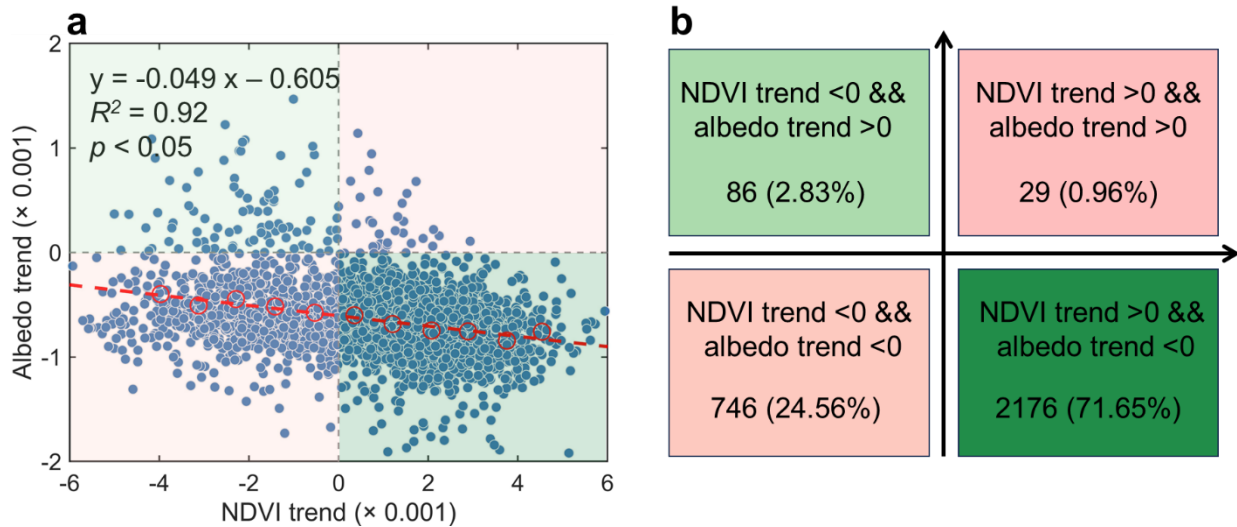
495 Intra-city associations (within cities) between urban NDVI and albedo trends show a total of 2564
 496 cities are negatively correlated (**Fig. 8**), with 583, 1077, and 904 cities presenting correlation
 497 coefficients < -0.6 , within the -0.6 to -0.3 , and -0.3 to 0 ranges, respectively. Only 291 of 473 cities
 498 have statistically significant positive NDVI-albedo relationships, most of which are distributed in
 499 Europe and East Asia. Inter-city associations (across cities) using the median albedo trends derived
 500 from 10% NDVI bins show that the increase in NDVI trend (with a slope of -0.049) coexists with
 501 the decrease in albedo trend, which explains 92% of the total variance of the albedo binned trend
 502 (**Fig. 9a**). Moreover, statistical results of NDVI and albedo trend consistency from the raw
 503 observations show a decrease in albedo trend of 2176 (71.65%) cities in the opposite direction

504 with respect to the NDVI trend (**Fig. 9b**). As the greening trend is greater (0.004 yr^{-1}) for the past
 505 21 years (**Fig. S8**), the intra- and inter-city associations between urban NDVI and albedo trends
 506 become stronger, with more cities exhibiting negative NDVI-albedo correlation coefficients (**Figs.**
 507 **S9 and S10**). These intra- and inter-city dominant negative associations reveal that urban greening
 508 will lead to a decreasing albedo trend.

509
 510



512 **Fig. 8.** Spatial patterns of the intra-city correlation between urban normalized difference vegetation
 513 index (NDVI) and albedo trend for 3037 global cities over 35 years (1986-2020), with the
 514 histogram (correlation coefficient key) of the city-level albedo trend and the number of cities (with
 515 the associated percentage in parentheses) given above the inserted histogram. Large markers
 516 represent a statistical significance level of 0.05 (p -value < 0.05) and small markers represent a non-
 517 significant trend with p -value > 0.05 .



518

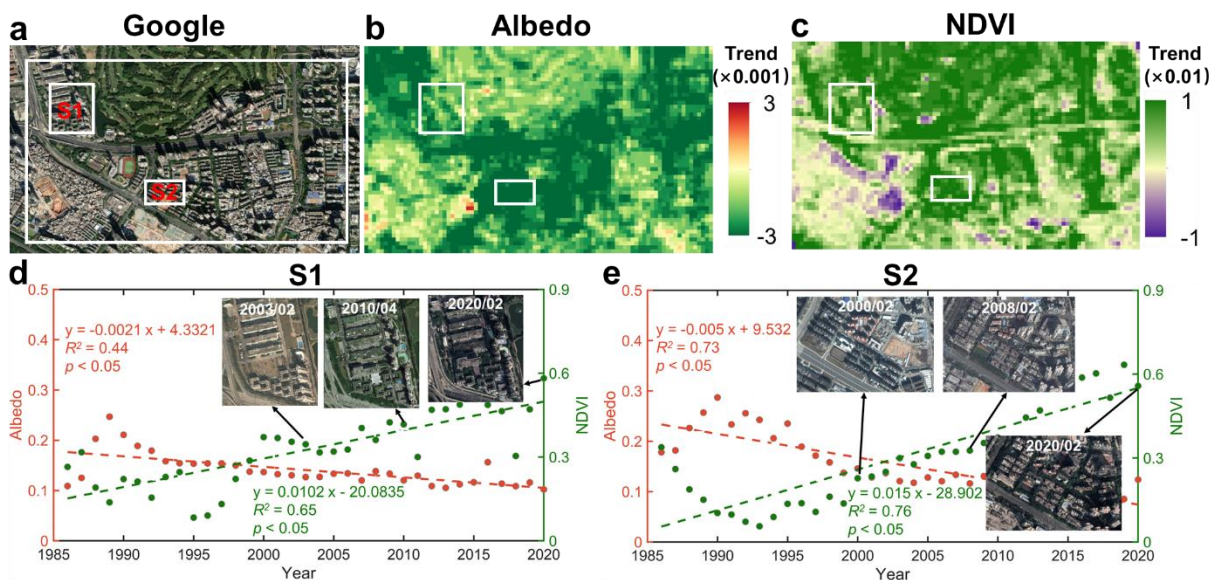
519 **Fig. 9.** Associations between city-level normalized difference vegetation index (NDVI) and
 520 surface albedo trends for 3037 global cities over 35 years (1986-2020), with (a) scatter plot and
 521 (b) statistics of NDVI and albedo trend consistency. In (a), the city-level trends are averaged from
 522 pixel-level trends that are statistically significant at a level of 0.05, using the non-parametric Mann-
 523 Kendall and Theil–Sen slope estimator approaches. A zonal analysis is used to refine the
 524 association results by averaging the NDVI and albedo trend pairs (red circles) within each 10%
 525 NDVI interval for the linear regression (red dashed line).

526

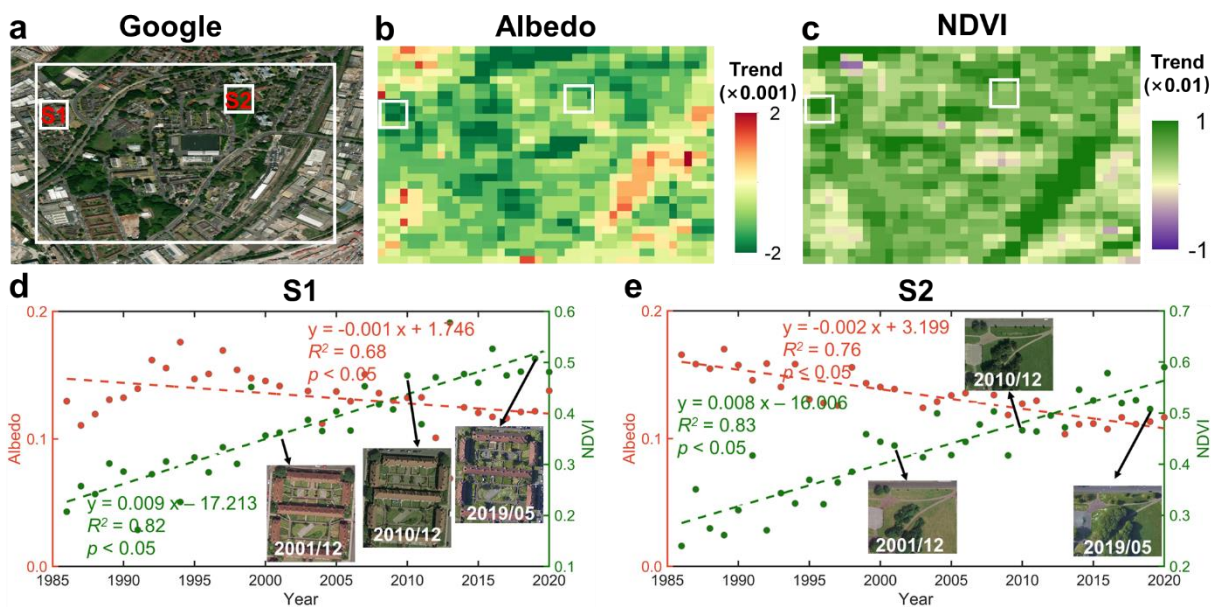
527

528 Four sample cities provide spatially explicit information on the decreasing trend of surface albedo
 529 caused by different greening pathways: tree planting (Shenzhen, China and Birmingham, United
 530 Kingdom) and urban warming-induced vegetation growth (Milton, Florida and Pinehurst, North
 531 Carolina, United States). Shenzhen and Birmingham have experienced tremendous urbanization
 532 during the past three decades, but they have also implemented tree planting programs in central
 533 areas, as it can be observed through the NDVI trend maps and high-resolution Google Earth
 534 satellite images (**Fig. 10a-c** and **Fig. 11a-c**). Two local sites in both Shenzhen and Birmingham
 535 clearly show the opposite trends for the NDVI and albedo time series (**Fig. 10d-e** and **Fig. 11d-e**).
 536 In comparison, Milton and Pinehurst are two well-urbanized cities without substantial impervious
 537 area expansion in the urban fringe areas. Despite the absence of large-area tree planting activities,
 538 greenness continues to increase in these two cities due to enhanced vegetation growth induced by
 539 urban warming (**Figs. 12** and **13**). The significant negative correlation between surface albedo and
 540 2-D (NDVI as vegetation coverage) and 3-D (vegetation height) vegetation structure metrics in the
 541 baseline year 2020 further explains the multifaceted controls of urban greening on surface albedo
 542 (**Fig. 14**). Besides urban greening, the other anthropogenic practices might influence surface

543 albedo variations. For example, as shown in **Figs. S11** and **S12**, building construction and rooftop
 544 renewal with new light-color materials increase surface albedo. Nevertheless, the frequency and
 545 intensity of building construction is lower than urban vegetation growth, which results in the
 546 greening-dominated declining trend of urban surface albedo worldwide.
 547

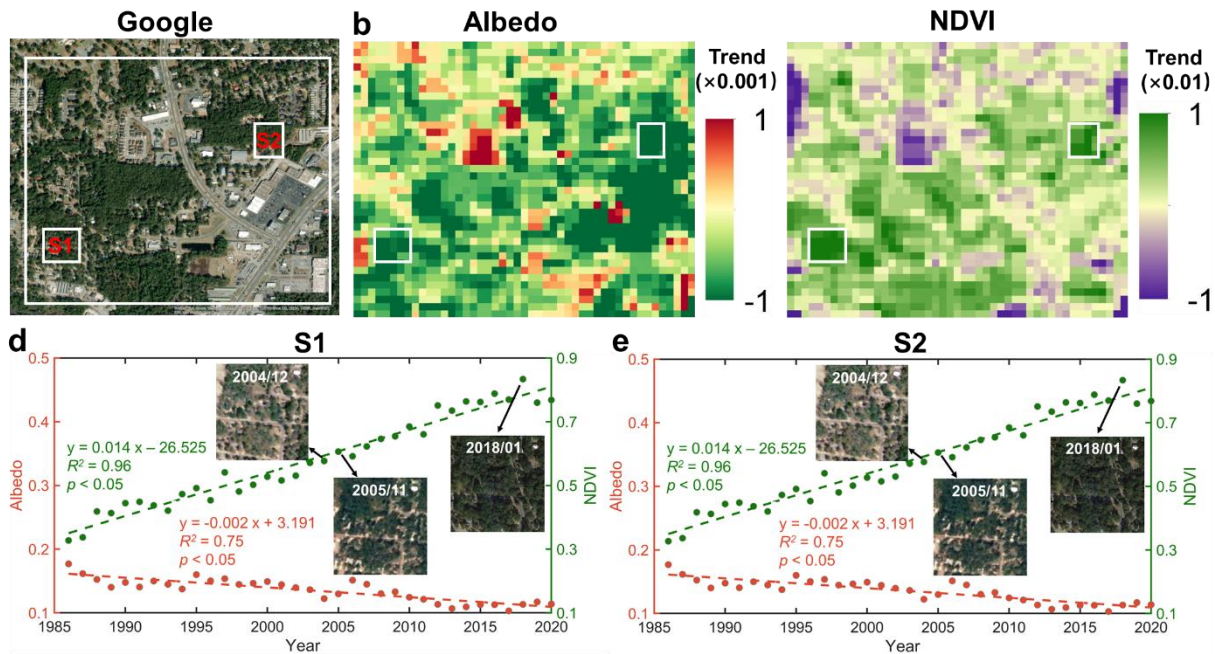


548 **Fig. 10.** Examples showing the close association between surface albedo and urban greening in
 549 the Shenzhen city, China, based on the maps of (a) Google Earth satellite image, (b) albedo trend,
 550 (c) NDVI trend, (d) time series of urban NDVI and albedo for S1 area in (a), and (e) time series
 551 of urban NDVI and albedo for S2 area in (a).
 552
 553

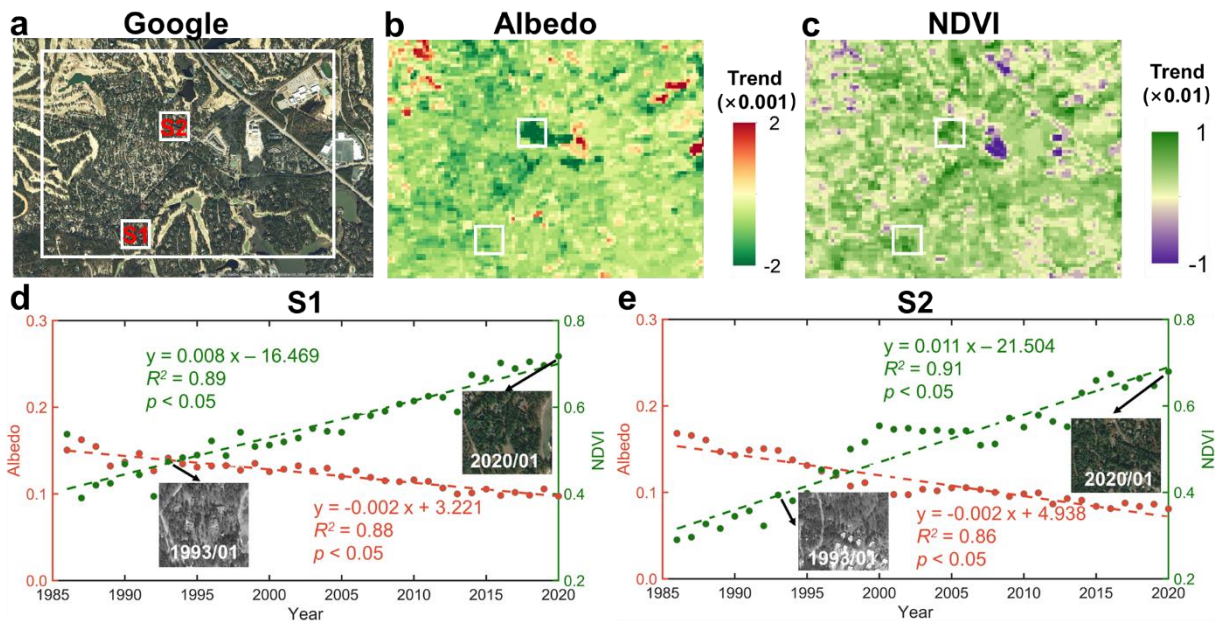


554

555 **Fig. 11.** Examples showing the close association between surface albedo and urban greening in the
 556 Birmingham city, United Kingdom, based on the maps of (a) Google Earth satellite image, (b)
 557 albedo trend, (c) NDVI trend, (d) time series of urban NDVI and albedo for S1 area in (a), and (e)
 558 time series of urban NDVI and albedo for S2 area in (a).
 559

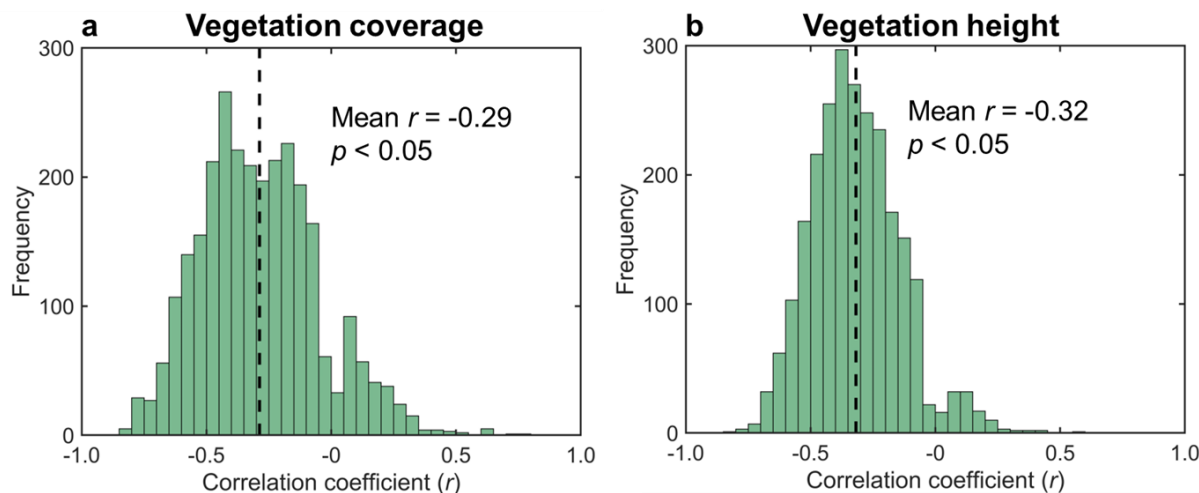


560
 561 **Fig. 12.** Examples of close association between surface albedo and urban greening in the Milton
 562 city, Florida, United States, based on the maps of (a) Google Earth satellite image, (b) albedo trend,
 563 (c) NDVI trend, (d) time series of urban NDVI and albedo for the S1 area in (a), and (e) time series
 564 of urban NDVI and albedo for the S2 area in (a).



565
 23

566 **Fig. 13.** Examples of close association between surface albedo and urban greening in the Pinehurst
 567 city, North Carolina, based on the maps of (a) Google Earth satellite image, (b) albedo trend, (c)
 568 NDVI trend, (d) time series of urban NDVI and albedo for the S1 area in (a), and (e) time series
 569 of urban NDVI and albedo for the S2 area in (a).
 570

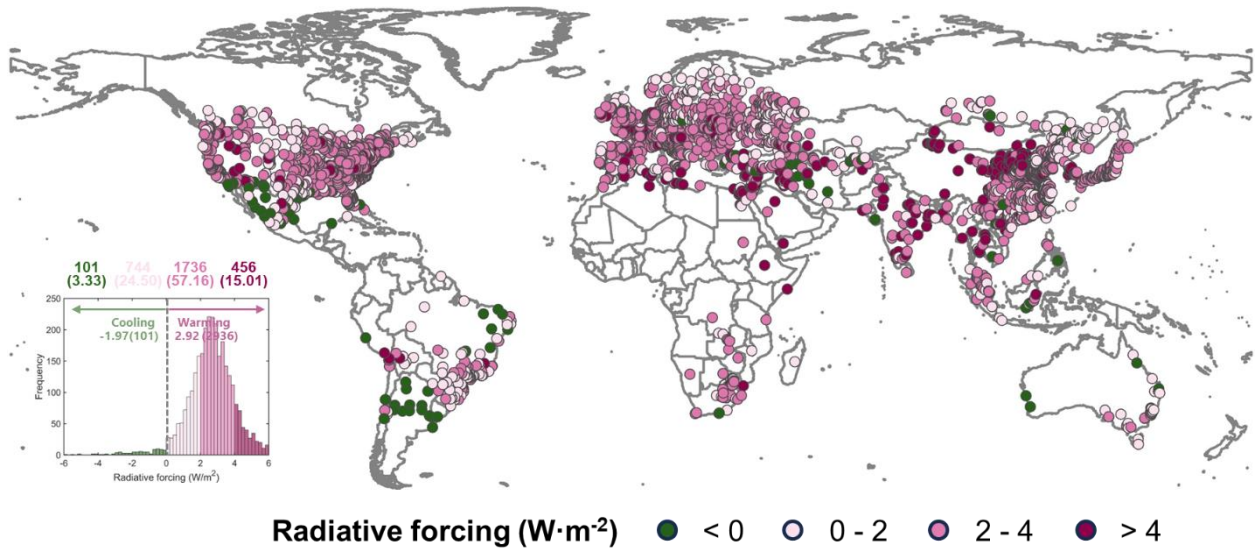


571
 572 **Fig. 14.** Correlation between surface albedo and (a) 30-m-resolution Landsat normalized
 573 difference vegetation index (NDVI, Gorelick et al. 2017), and (b) 10-m-resolution vegetation
 574 height (Lang et al. 2023) of the baseline year 2020 for 3037 global cities.
 575

576 4.4. Global variations of albedo-induced urban surface radiative forcing

577 The 35-year change in surface albedo has caused a mean positive surface radiative forcing of 2.76
 578 $\pm 1.92 \text{ W}\cdot\text{m}^{-2}$ for the 3037 global cities assessed in this study (**Fig. 15**), suggesting a net increase
 579 in absorbed incoming solar energy at the urban surface. Large inter-city spatial variabilities are
 580 observed, with values ranging from -10.75 to 23.34 $\text{W}\cdot\text{m}^{-2}$. The 2936 cities with positive radiative
 581 forcing (i.e., warming) have a mean value of 2.92 $\text{W}\cdot\text{m}^{-2}$, while the 101 cities with negative
 582 radiative forcing have a mean value of -1.97 $\text{W}\cdot\text{m}^{-2}$. The mean magnitude of albedo-induced
 583 radiative forcing also varies by regions: 3.14 $\text{W}\cdot\text{m}^{-2}$ for 1073 Asian cities; 3.09 $\text{W}\cdot\text{m}^{-2}$ for 92
 584 African cities; 2.72 $\text{W}\cdot\text{m}^{-2}$ for 933 European cities; 2.60 $\text{W}\cdot\text{m}^{-2}$ for 789 North American cities; 1.23
 585 $\text{W}\cdot\text{m}^{-2}$ for 31 Australian cities; and 0.85 $\text{W}\cdot\text{m}^{-2}$ for 119 South American cities.

586



587
 588 **Fig. 15.** Spatial patterns of surface radiative forcing (RF, $W \cdot m^{-2}$) from albedo change for 3037
 589 global cities over 35 years (1986-2020), with the number of cities (and the associated percentage
 590 in parentheses) given above the inserted histogram.
 591

592

593

5. Discussion

594

5.1. Uncertainty analysis

596 Some influencing factors such as training sample representativeness, Landsat data uncertainty,
 597 seasonal variation, building footprint, and snow event may mislead our findings. To examine their
 598 impacts, we conducted sensitivity analyses and discussed the potential uncertainties associated
 599 with each of these factors.

600

5.1.1. Training sample representativeness

602 The representativeness of training samples, angular-bin size, and regression relationship between
 603 reflectance and albedo are three factors that need to be considered for the successful application
 604 of the direct estimation approach. Recent studies have thoroughly investigated the sensitivity to
 605 the angular-bin size and the regression relationship between reflectance and albedo, verifying their
 606 applicability to both natural and urban surfaces (Chen et al. 2023; Lin et al. 2022). Therefore,
 607 training dataset representativeness has been highlighted as a key component for the application of
 608 the direct estimation approach over urban areas. We conducted two sensitivity analyses using

609 BRDF/albedo over mixed land covers (16 IGBP land covers used in this study, referred to as
610 general scheme) and pure urban cover (referred to as urban scheme) to test the theoretical accuracy
611 of this approach over urban areas. Results show that these two schemes have almost the same
612 theoretical accuracy (0.0161 vs. 0.0156, **Fig. S13**), which is very close to the MODIS
613 BRDF/albedo product accuracy (Wang et al. 2018). Based on the optimized BRDF/albedo training
614 samples for the general scheme (7200 samples for 16 land covers with 450 samples per type) and
615 urban scheme (3000 urban cover samples), we constructed one general and one urban reflectance-
616 to-albedo LUT and validated their accuracy with global flux tower-based measurements.
617 Validation results reveal that these two algorithms are highly accurate, suggesting that the direct
618 estimation approach used in this study with the general training sample scheme is stable (**Fig. 4 vs.**
619 **Fig. S14**).

620

621 **5.1.2. Landsat data uncertainty**

622 The uncertainty of Landsat data quality mainly stems from Landsat satellite orbital drifts and scan
623 line corrector (SLC) failure in Landsat-7. On the one hand, Landsat satellite orbital drifts (e.g.,
624 Landsat-5 drifted between 1995-2000 and 2003-2007, Landsat-7 drifted from 2017 to the present;
625 Qiu et al. 2021; Zhang and Roy, 2016) alter local acquisition time, affecting solar-viewing
626 geometry and surface reflectance, resulting in artificial impacts on surface albedo. To minimize
627 such impacts, we trained the spectral reflectance with shortwave albedo at local solar noon (e.g.,
628 12:00 p.m.) to construct reflectance-to-albedo LUTs, allowing us to compare predicted surface
629 albedo across years (Guo et al. 2022). On the other hand, since Landsat-7 data covers only two
630 years (2012-2013), the data gap impacts from this satellite on the main findings of this study are
631 minor. Sensitivity analysis shows that the yearly mean and long-term temporal trend of global
632 urban albedo are nearly the same, whether or not Landsat-7 satellite data are used (**Figs. 5-6 vs.**
633 **Fig. S15**).

634

635 **5.1.3. Seasonal variation**

636 Seasonal impacts on urban albedo estimation and analysis come from two sources: seasonal
637 vegetation growth and seasonal solar geometry change. On the one hand, Landsat satellite has a
638 regular 16-day revisit cycle, which allows at least two observations per month to capture seasonal

639 vegetation growth dynamics. On the other hand, our algorithm has normalized surface albedo to
640 local solar noon and the solar position is relatively stable within a month, minimizing the
641 interference from seasonal change of solar geometry. Sensitivity analysis results of the Landsat-
642 derived albedo trends using time series from different seasons are very similar to those of the
643 annual mean time series (**Fig. S16**), supporting the minor seasonal variation effects on the observed
644 decreasing albedo trend of global urban cities in this study.

645 **5.1.4. Building footprint**

646 Building footprint changes, such as those related to new construction or building renovations using
647 different materials, might increase urban albedo (**Figs. S11 and S12**). To explore building footprint
648 impacts on surface albedo, we used 30-m-resolution rasterized building footprint (i.e., total,
649 average, minimum, and maximum building areas within a 30-m-resolution pixel) dataset for 242
650 cities in the United States (Heris et al. 2020), and three building height datasets for China (120
651 cities; Yang and Zhao et al. 2022), Germany (18 cities; Frantz et al. 2021), and the United States
652 (372 cities; Falcone, 2016) to provide the horizontal and vertical building footprint metrics (**Table**
653 **S2**). By conducting a bivariate relationship analysis between building footprint metrics and albedo,
654 we found a positive correlation with mean correlation coefficients of 0.21, 0.21, 0.21, and 0.16 for
655 maximum (i.e., area of the largest building intersecting each 30-m pixel), minimum (i.e., area of
656 the smallest building intersecting each 30-m pixel), average (i.e., number of buildings that intersect
657 each 30-m pixel), and total (i.e., total building footprint coverage per 30-m pixel) building areas,
658 respectively (**Fig. S17**). We also observed a negative correlation between albedo and building
659 height, with a mean correlation coefficient of -0.22 (**Fig. S18**), as shadowing and radiative trapping
660 in canyons increase with building height. However, quantifying the contribution of the building
661 landscape to albedo change remains a challenging task due to the lack of high-resolution urban
662 building time-series products, which requires future investigation.

663

664 **5.1.5. Snow cover impact**

665 Snow cover is another important confounding factor for the spatiotemporal analysis of global
666 urban albedo due to its much higher reflectance than other urban materials. On one hand, because
667 regular snow events only occur for short periods in the winter for high-latitude cities, they will
668 have little impact on the general diminishing patterns of global urban albedo. Snow episodes, on

669 the other hand, are rather regular across time, and their influence on long-term urban albedo is
670 likely to be systematically linear, which will not modify the spatiotemporal trend analysis. Our
671 sensitivity analysis results demonstrate that, with the exception of a few high-latitude Northern
672 hemisphere cities, the overall decreasing trends of worldwide urban albedo are nearly the same
673 whether snowy satellite pixels are excluded or not (**Fig. 6** and **S19**).

674

675 **5.2. Novelty and implication of this study**

676 This study makes several advances over past similar studies on methodological development. First,
677 we investigated the direct estimation approach and validated its theoretical capability for retrieving
678 surface albedo from Landsat over global urban areas. Our training sample representativeness
679 sensitivity analyses indicate that more accurate urban BRDF/albedo training datasets beyond
680 MODIS are one potential way to improve the algorithm accuracy, which should include fine-
681 resolution 3-D radiative transfer model parameterization and global 3-D urban morphology
682 datasets. Second, the absolute accuracy of the direct estimation approach for estimating urban
683 albedo had not yet been properly evaluated. For the first time, this study used albedo data from
684 incoming and outgoing shortwave radiation measured by synthesized global urban flux towers
685 around the world as ground truth to assess the accuracy of the proposed algorithm. The results
686 demonstrated that Landsat-derived urban albedo is reliable (**Fig. 4**).

687

688 The global 35-year, 30-m-resolution urban surface albedo dataset generated in this study is unique
689 and valuable. Although many previous efforts have attempted to estimate surface albedo from
690 high-resolution Sentinel-2 and Landsat satellite data (Guo et al. 2022; He et al. 2018; Lin et al.
691 2022; Shuai et al. 2011; 2014), most of them were limited to individual locations, cities, or specific
692 regions, and years, which hampered our understanding of the spatiotemporal patterns of global
693 urban albedo throughout the past three decades of urbanization. Our albedo dataset of 3037 cities
694 from around the world, including cities in the Global North and Global South, provides us a
695 thorough picture of the dynamic spatiotemporal evolution of global urban albedo. This dataset can
696 be incorporated as input data into urban canopy models (Ryu et al. 2016) for the monitoring and
697 estimation of urban energy balance and other albedo-related studies.

698

699 By comparing the results of the previous three decades with those of the previous two decades
700 using the global 30-m resolution Landsat albedo dataset developed here, we found that global
701 urban albedo is decreasing at an increasing rate, implying that the albedo-induced warming has
702 been exacerbated. We also observed that the urban greening phenomenon is expanding around the
703 globe. Since 1985, 72.60% of global cities (2205) have increased greening, and this proportion has
704 increased to 89.20% (2709 cities) since 2001. This proportion is higher than the 70% reported in
705 a previous study using coarse-resolution MODIS data (Zhang et al. 2021). Finally, our study
706 demonstrates that urban greening regulates the decreasing trend of urban albedo through two
707 different pathways: tree planting and urban warming-enhanced vegetation growth. These findings
708 help to clarify recent controversial conclusions about worldwide urban albedo trend patterns (Guo
709 et al. 2022; Ouyang et al. 2022). Guo et al. (2022) reported an increasing trend of urban albedo
710 based on 30-m resolution Landsat-derived summer albedo across 11 Chinese megacities, without
711 taking into account the various urbanization trends in other Chinese cities or around the world, as
712 well as seasonal changes. By comparing the 1°-resolution albedo estimated from MODIS land
713 cover types across two baseline years, 2018 and 2001, Ouyang et al. (2022) found a decreasing
714 pattern in urban areas. This coarse-resolution and short-term data (since 2001) cannot detect fine-
715 scale heterogeneity in the urbanization processes during the past three decades, such as tree
716 planting and construction of new buildings and roads, as well as changes in existing artificial
717 impervious surfaces. Using our 30-m resolution surface albedo and NDVI dataset covering 3037
718 cities around the world, we determined that greening is the key controlling factor for the downward
719 trend of urban albedo using multidimensional association analysis and further evidence from local
720 cases.

721
722 The strong relationship between urban greening and albedo has important implications. Planting
723 trees, in conjunction with artificial albedo alterations (e.g., the use of high-reflective materials),
724 have been recognized as two critical approaches to mitigate urban warming (Chen et al. 2022;
725 Wong et al. 2021). However, albedo-induced warming effects of urban greening have received
726 little attention. Recent vegetation greening research at regional and global scales have found that
727 albedo is a key component in the greening-induced change in the Earth's energy budget and might
728 potentially offset cooling benefits, causing local and global warming (Lian et al. 2022; Piao et al.
729 2020). This study provides empirical evidence of the warming effect triggered by changes in urban

730 albedo caused by increased vegetation, a phenomenon that must be taken into account when
731 evaluating the effectiveness of greening-based cooling solutions by incorporating such fine-scale
732 datasets with 3-D microclimate models (e.g., SOLWEIG; Lindberg et al. 2008).

733

734 **5.3. Limitations and future perspectives**

735 It is important to recognize and resolve various limitations and uncertainties in this study for future
736 research. Topography is an essential factor in estimating albedo, although it has seldom been taken
737 into account when mapping surface albedo on a wide scale using satellite data. In this study, we
738 do not include topography, as the majority of the cities investigated exhibit minimal variations in
739 elevation (mean slope = 3.3° , **Fig. S20**). But some cities have large slopes, and their surface albedo
740 retrieval may still require accounting for topographic impacts (Wu et al. 2018, 2019).

741

742 Another critical issue to address is 3-D urban morphology, which requires significantly higher
743 resolution data (e.g., ~ 1 m) for both the satellite surface reflectance and morphology datasets. The
744 impact of urban geometry, such as the density of buildings, the sky view factor, and the aspect
745 ratio of buildings, on surface albedo, and in turn on air temperature close to the surface is widely
746 recognized (Xu et al. 2020; Yang and Li, 2015). The increasing availability of high-resolution
747 Digital Surface Model data (e.g., Scott et al. 2022) and 3-D building data (e.g., Zhou et al. 2022)
748 will strengthen interpretation of higher-resolution satellite observations beyond Landsat (e.g., 10-
749 m Sentinel-2 with ~ 5 -day revisit; 3-m PlanetScope with daily revisit; Drusch et al. 2012; Planet
750 Team, 2022) to improve albedo estimates at urban facet scale (e.g., road, roof, and wall).

751

752 Although fine-scale albedo trends have been studied, Landsat data remains a mixed signal that
753 cannot effectively segregate individual contributions from different urban elements (e.g., building,
754 tree, and grassland) to the overall spatiotemporal trend of urban albedo. Furthermore, the
755 individual contributions of tree planting and urban warming-enhanced vegetation growth to
756 greening-induced urban albedo modification are still unknown. An integration of fine-resolution
757 land-cover datasets of different urban elements and high-resolution albedo datasets are expected
758 to be used for isolating and assessing the individual contributions of particular urban features.
759 Finally, this study did not take into account the detailed spatial and temporal variations associated
760 with land cover changes, which can be analyzed by combining our Landsat albedo data with the

761 appropriate high-resolution annual land cover map data. This will be helpful for city climate
762 change management to address mitigation, adaptation, and forecasting because it directly affects
763 surface energy balance (Duveiller et al. 2018; Oke 1982).

764

765 **6. Conclusions**

766 The spatial and temporal features of urban surface albedo in cities around the world and their
767 underlying drivers are still not well understood due to a lack of high-resolution albedo observations.
768 In this study, we generated a 35-year, 30-m resolution annual albedo dataset for 3037 worldwide
769 cities. We demonstrated the accuracy and reliability of the albedo dataset by comparing it to albedo
770 data derived from flux tower-based measurements. We investigated the spatial and temporal
771 patterns and trends of urban albedo using this dataset and found that most cities had a decreasing
772 albedo trend as a consequence of increased greenness. Cities with this decrease in albedo are
773 expected to experience more (positive) surface radiative forcing.

774

775 **Acknowledgments**

776 This work was supported by the Open Fund of State Key Laboratory of Remote Sensing Science
777 under Grant No. OFSLRSS202017 awarded to S.W. X. L. was supported by the Chinese National
778 Natural Science Foundation Project (#41901290). Q.L. was supported by the Major Key Project
779 of Pengcheng Laboratory. B.C. was supported by The University of Hong Kong HKU-100 Scholar
780 Fund and Seed Fund for Strategic Interdisciplinary Research Scheme. The Landsat surface
781 reflectance and MODIS BRDF/albedo product are available from the Google Earth Engine (GEE)
782 cloud-computing platform. The Urban-PLUMBER flux tower datasets are available from
783 <https://doi.org/10.5281/zenodo.6590886>. The URBANFLUXES flux tower datasets are available
784 from <http://urbanfluxes.eu/>. The monthly BaRAD solar radiation dataset is available from
785 <https://doi.org/10.1594/PANGAEA.932924>. The authors would like to thank all PIs of urban flux
786 towers providing valuable flux datasets.

787

788 **References**

789 Akbari, H., Matthews, H.D., Seto, D. 2012. The long-term effect of increasing the albedo of urban
790 areas. *Environmental Research Letters*, 7, 024004

791 Beck, H.E., Zimmermann, N.E., McVicar, T.R., Vergopolan, N., Berg, A., Wood, E.F. 2018.
792 Present and future Köppen-Geiger climate classification maps at 1-km resolution. *Scientific*
793 *Data*, 5, 1-12

794 Bjorkegren, A., Grimmond, C.S.B., Kotthaus, S., Malamud, B. 2015. CO₂ emission estimation in
795 the urban environment: Measurement of the CO₂ storage term. *Atmospheric Environment*,
796 122, 775-790

797 Bonafoni, S., Sekertekin, A. 2020. Albedo retrieval from Sentinel-2 by new narrow-to-broadband
798 conversion coefficients. *IEEE Geoscience and Remote Sensing Letters*, 17, 1618-1622

799 Buchhorn, M., Lesiv, M., Tsendbazar, N.-E., Herold, M., Bertels, L., Smets, B. 2020. Copernicus
800 global land cover layers—collection 2. *Remote Sensing*, 12, 1044

801 Cao, C., Lee, X., Liu, S., Schultz, N., Xiao, W., Zhang, M., Zhao, L. 2016. Urban heat islands in
802 China enhanced by haze pollution. *Nature Communications*, 7, 1-7

803 Chakraborty, T., Lee, X. 2021. Using supervised learning to develop BaRAD, a 40-year monthly
804 bias-adjusted global gridded radiation dataset. *Scientific Data*, 8, 1-10

805 Chen, B., Wu, S., Song, Y., Webster, C., Xu, B., Gong, P. 2022. Contrasting inequality in human
806 exposure to greenspace between cities of Global North and Global South. *Nature*
807 *Communications*, 13, 1-9

808 Chen, H., Lin, X., Sun, Y., Wen, J., Wu, X., You, D., Cheng, J., Zhang, Z., Zhang, Z., Wu, C.
809 2023. Performance Assessment of Four Data-Driven Machine Learning Models: A Case to
810 Generate Sentinel-2 Albedo at 10 Meters. *Remote Sensing*, 15, 2684

811 Chen, X., Liang, S., Cao, Y., He, T., Wang, D. 2015. Observed contrast changes in snow cover
812 phenology in northern middle and high latitudes from 2001–2014. *Scientific Report*, 5, 1-9

813 Chow, W. 2017. Eddy covariance data measured at the CAP LTER flux tower located in the west
814 Phoenix, AZ neighborhood of Maryvale from 2011-12-16 through 2012-12-31

815 Christen, A., Vogt, R. 2004. Energy and radiation balance of a central European city. *International*
816 *Journal of Climatology: A Journal of the Royal Meteorological Society*, 24, 1395-1421

817 Chrysoulakis, N., Grimmond, S., Feigenwinter, C., Lindberg, F., Gastellu-Etchegorry, J.-P.,
818 Marconcini, M., Mitraka, Z., Stagakis, S., Crawford, B., Olofson, F. 2018. Urban energy
819 exchanges monitoring from space. *Scientific Report*, 8, 1-8

820 Coutts, A.M., Beringer, J., Tapper, N.J. 2007. Characteristics influencing the variability of urban
821 CO₂ fluxes in Melbourne, Australia. *Atmospheric Environment*, 41, 51-62

822 Crawford, B., Christen, A. 2015. Spatial source attribution of measured urban eddy covariance
823 CO₂ fluxes. *Theoretical and Applied Climatology*, 119, 733-755

824 Crawford, B., Grimmond, C., Christen, A. 2011. Five years of carbon dioxide fluxes measurements
825 in a highly vegetated suburban area. *Atmospheric Environment*, 45, 896-905

826 Drusch, M., Del Bello, U., Carlier, S., Colin, O., Fernandez, V., Gascon, F., Hoersch, B., Isola, C.,
827 Laberinti, P., Martimort, P. 2012. Sentinel-2: ESA's optical high-resolution mission for
828 GMES operational services. *Remote Sensing of Environment*, 120, 25-36

829 Duveiller, G., Hooker, J., Cescatti, A. 2018. The mark of vegetation change on Earth's surface
830 energy balance. *Nature Communications*, 9, 1-12

831 Estoque, R.C., Ooba, M., Seposo, X.T., Togawa, T., Hijjoka, Y., Takahashi, K., Nakamura, S.
832 2020. Heat health risk assessment in Philippine cities using remotely sensed data and social-
833 ecological indicators. *Nature Communications*, 11, 1-12

834 Falasca, S., Ciancio, V., Salata, F., Golasi, I., Rosso, F., Curci, G. 2019. High albedo materials to
835 counteract heat waves in cities: An assessment of meteorology, buildings energy needs and
836 pedestrian thermal comfort. *Building and Environment*, 163, 106242

837 Falcone, J.A. 2016. US national categorical mapping of building heights by block group from
838 Shuttle Radar Topography Mission data. <http://dx.doi.org/10.5066/F7W09416>

839 Feigenwinter, C., Vogt, R., Parlow, E., Lindberg, F., Marconcini, M., Del Frate, F., Chrysoulakis,
840 N. 2018. Spatial distribution of sensible and latent heat flux in the city of Basel (Switzerland).
841 *IEEE Journal of Selected Topics in Applied Earth Observations and Remote Sensing*, 11,
842 2717-2723

843 Fortuniak, K., Pawlak, W., Siedlecki, M. 2013. Integral turbulence statistics over a central
844 European city centre. *Boundary-layer meteorology*, 146, 257-276

845 Frantz, D., Schug, F., Okujeni, A., Navacchi, C., Wagner, W., van der Linden, S., Hostert, P. 2021.
846 National-scale mapping of building height using Sentinel-1 and Sentinel-2 time series.
847 *Remote Sensing of Environment*, 252, 11212

848 Ghimire, B., Williams, C.A., Masek, J., Gao, F., Wang, Z., Schaaf, C., He, T. 2014. Global albedo
849 change and radiative cooling from anthropogenic land cover change, 1700 to 2005 based on
850 MODIS, land use harmonization, radiative kernels, and reanalysis. *Geophysical Research*
851 *Letters*, 41, 9087-9096

852 Gorelick, N., Hancher, M., Dixon, M., Iyushchenko, S., Thau, D., Moore, R. 2017. Google Earth
853 Engine: Planetary-scale geospatial analysis for everyone. *Remote Sensing of Environment*,
854 202, 18-27

855 Goret, M., Masson, V., Schoetter, R., Moine, M.-P. 2019. Inclusion of CO2 flux modelling in an
856 urban canopy layer model and an evaluation over an old European city centre. *Atmospheric*
857 *Environment: X*, 3, 100042

858 Groleau, D., Mestayer, P.G. 2013. Urban morphology influence on urban albedo: A revisit with
859 the SOLENE model. *Boundary-layer meteorology*, 147, 301-327

860 Guo, T., He, T., Liang, S., Roujean, J.-L., Zhou, Y., Huang, X. 2022. Multi-decadal analysis of
861 high-resolution albedo changes induced by urbanization over contrasted Chinese cities based
862 on Landsat data. *Remote Sensing of Environment*, 269, 112832

863 Heris, M.P., Foks, N.L., Bagstad, K.J., Troy, A., Ancona, Z.H. 2020. A rasterized building
864 footprint dataset for the United States. *Scientific Data*, 7, 1-10

865 He, T., Liang, S., Wang, D., Cao, Y., Gao, F., Yu, Y., Feng, M. 2018. Evaluating land surface
866 albedo estimation from Landsat MSS, TM, ETM+, and OLI data based on the unified direct
867 estimation approach. *Remote Sensing of Environment*, 204, 181-196

868 Hong, J., Lee, K., and Hong, J.-W.: Observational data of Ochang and Jungnang in Korea, 2020

869 Hsu, A., Sheriff, G., Chakraborty, T., Manya, D. 2021. Disproportionate exposure to urban heat
870 island intensity across major US cities. *Nature Communications*, 12, 1-11

871 Hu, Y., Jia, G., Pohl, C., Zhang, X., van Genderen, J. 2016. Assessing surface albedo change and
872 its induced radiation budget under rapid urbanization with Landsat and GLASS data.
873 *Theoretical and Applied Climatology*, 123, 711-722

874 Huang, H., Xin, D., Hailin, Y., Xinhui, Z., Qi, J. 2020. Spatio-temporal mechanism underlying the
875 effect of urban heat island on cardiovascular diseases. *Iranian Journal of Public Health*, 49,
876 1455

877 Hwang, Y., Ryu, Y., Qu, S. 2022. Expanding vegetated areas by human activities and
878 strengthening vegetation growth concurrently explain the greening of Seoul. *Landscape and*
879 *Urban Planning*, 227, 104518

880 Ishidoya, S., Sugawara, H., Terao, Y., Kaneyasu, N., Aoki, N., Tsuboi, K., Kondo, H. 2020. O₂:
881 CO₂ exchange ratio for net turbulent flux observed in an urban area of Tokyo, Japan, and its
882 application to an evaluation of anthropogenic CO₂ emissions. *Atmospheric Chemistry and*
883 *Physics*, 20, 5293-5308

884 Järvi, L., Rannik, Ü., Kokkonen, T.V., Kurppa, M., Karppinen, A., Kouznetsov, R.D., Rantala, P.,
885 Vesala, T., Wood, C.R. 2018. Uncertainty of eddy covariance flux measurements over an
886 urban area based on two towers. *Atmospheric Measurement Techniques*, 11, 5421-5438

887 Karsisto, P., Fortelius, C., Demuzere, M., Grimmond, C.S.B., Oleson, K., Kouznetsov, R., Masson,
888 V., Järvi, L. 2016. Seasonal surface urban energy balance and wintertime stability simulated
889 using three land-surface models in the high-latitude city Helsinki. *Quarterly Journal of the*
890 *Royal Meteorological Society*, 142, 401-417

891 Kuang, W., Liu, A., Dou, Y., Li, G., Lu, D. 2019. Examining the impacts of urbanization on surface
892 radiation using Landsat imagery. *GIScience & Remote Sensing*, 56, 462-484

893 Lang, N., Jetz, W., Schindler, K., Wegner, J.D. 2023. A high-resolution canopy height model of
894 the Earth. *Nature Ecology & Evolution*, 7, 1778–1789

895 Lian, X., Jeong, S., Park, C.-E., Xu, H., Li, L.Z., Wang, T., Gentine, P., Peñuelas, J., Piao, S. 2022.
896 Biophysical impacts of northern vegetation changes on seasonal warming patterns. *Nature*
897 *Communications*, 13, 3925

898 Li, X., Gong, P., Zhou, Y., Wang, J., Bai, Y., Chen, B., Hu, T., Xiao, Y., Xu, B., Yang, J. 2020.
899 Mapping global urban boundaries from the global artificial impervious area (GAIA) data.
900 *Environmental Research Letters*, 15, 094044

901 Liang, S., Fang, H., Chen, M., Shuey, C.J., Walthall, C., Daughtry, C., Morisette, J., Schaaf, C.,
902 Strahler, A. 2002. Validating MODIS land surface reflectance and albedo products: Methods
903 and preliminary results. *Remote Sensing of Environment*, 83, 149-162

904 Lin, X., Wu, S., Chen, B., Lin, Z., Yan, Z., Chen, X., Yin, G., You, D., Wen, J., Liu, Q. 2022.
905 Estimating 10-m land surface albedo from Sentinel-2 satellite observations using a direct
906 estimation approach with Google Earth Engine. *ISPRS Journal of Photogrammetry and*
907 *Remote Sensing*, 194, 1-20

908 Lindberg, F., Holmer, B., Thorsson, S. 2008. SOLWEIG 1.0—Modelling spatial variations of 3D
909 radiant fluxes and mean radiant temperature in complex urban settings. *International Journal*
910 *of Biometeorology*, 52, 697-713

911 Lipson et al. (2022a) <https://doi.org/10.5281/zenodo.7104984> (last accessed on November 6,
912 2022).

913 Lipson, M., Grimmond, S., Best, M., Chow, W., Christen, A., Chrysoulakis, N., Coutts, A.,
914 Crawford, B., Earl, S., Evans, J., Fortuniak, K., Heusinkveld, B. G., Hong, J.-W., Hong, J.,
915 Järvi, L., Jo, S., Kim, Y.-H., Kotthaus, S., Lee, K., Masson, V., McFadden, J. P., Michels, O.,
916 Pawlak, W., Roth, M., Sugawara, H., Tapper, N., Velasco, E., and Ward, H. C. (2022b):
917 Harmonized gap-filled datasets from 20 urban flux tower sites, *Earth System Science Data*,
918 14, 5157-5178

919 Liu, X., Huang, Y., Xu, X., Li, X., Li, X., Ciais, P., Lin, P., Gong, K., Ziegler, A.D., Chen, A.
920 2020. High-spatiotemporal-resolution mapping of global urban change from 1985 to 2015.
921 *Nature Sustainability*, 3, 564-570

922 Lucht, W., Schaaf, C.B., Strahler, A.H. 2000. An algorithm for the retrieval of albedo from space
923 using semiempirical BRDF models. *IEEE Transactions on Geoscience and Remote Sensing*,
924 38, 977-998

925 Mann, H. 1945. Non-parametric tests against trend. *Econometria*. In: Chicago

926 Meng, L., Mao, J., Zhou, Y., Richardson, A.D., Lee, X., Thornton, P.E., Ricciuto, D.M., Li, X.,
927 Dai, Y., Shi, X. 2020. Urban warming advances spring phenology but reduces the response
928 of phenology to temperature in the conterminous United States. *Proceedings of the National*
929 *Academy of Sciences*, 117, 4228-4233

930 Menon, S., Akbari, H., Mahanama, S., Sednev, I., Levinson, R. 2010. Radiative forcing and
931 temperature response to changes in urban albedos and associated CO₂ offsets. *Environmental*
932 *Research Letters*, 5, 014005

933 Morini, E., Touchaei, A.G., Castellani, B., Rossi, F., Cotana, F. 2016. The impact of albedo
934 increase to mitigate the urban heat island in Terni (Italy) using the WRF model. *Sustainability*,
935 8, 999

936 Myhre, G., Shindell, D., Pongratz, J. 2014. Anthropogenic and natural radiative forcing

937 Oke, T.R. 1982. The energetic basis of the urban heat island. *Quarterly Journal of the Royal*
938 *Meteorological Society*, 108, 1-24

939 Ouyang, Z., Sciusco, P., Jiao, T., Feron, S., Lei, C., Li, F., John, R., Fan, P., Li, X., Williams, C.A.
940 2022. Albedo changes caused by future urbanization contribute to global warming. *Nature*
941 *Communications*, 13, 1-9

942 Piao, S., Wang, X., Park, T., Chen, C., Lian, X., He, Y., Bjerke, J.W., Chen, A., Ciais, P.,
943 Tømmervik, H. 2020. Characteristics, drivers and feedbacks of global greening. *Nature*
944 *Reviews Earth & Environment*, 1, 14-27

945 Planet Team, Planet Imagery Product Specifications February 2021, Available online:
946 <https://www.planet.com/products/> (2022) (last accessed on November 6, 2022).

947 Qin, Y. 2015. Urban canyon albedo and its implication on the use of reflective cool pavements.
948 *Energy and Buildings*, 96, 86-94

949 Qiu, S., Zhu, Z., Shang, R., Crawford, C.J. 2021. Can Landsat 7 preserve its science capability
950 with a drifting orbit? *Science of Remote Sensing*, 4, 100026

951 Qu, Y., Liu, Q., Liang, S., Wang, L., Liu, N., Liu, S. 2013. Direct-estimation algorithm for
952 mapping daily land-surface broadband albedo from MODIS data. *IEEE Transactions on*
953 *Geoscience and Remote Sensing*, 52, 907-919

954 Rechid, D., Raddatz, T.J., Jacob, D. 2009. Parameterization of snow-free land surface albedo as a
955 function of vegetation phenology based on MODIS data and applied in climate modelling.
956 *Theoretical and Applied Climatology*, 95, 245-255

957 Ribeiro, H.V., Rybski, D., Kropp, J.P. 2019. Effects of changing population or density on urban
958 carbon dioxide emissions. *Nature Communications*, 10, 1-9

959 Rosso, F., Golasi, I., Castaldo, V.L., Piselli, C., Pisello, A.L., Salata, F., Ferrero, M., Cotana, F.,
960 de Lieto Vollaro, A. 2018. On the impact of innovative materials on outdoor thermal comfort
961 of pedestrians in historical urban canyons. *Renewable Energy*, 118, 825-839

962 Roth, M., Jansson, C., Velasco, E. 2017. Multi-year energy balance and carbon dioxide fluxes over
963 a residential neighbourhood in a tropical city. *International Journal of Climatology*, 37, 2679-
964 2698

965 Ryu, Y.-H., Bou-Zeid, E., Wang, Z.-H., & Smith, J.A. (2016). Realistic representation of trees in
966 an urban canopy model. *Boundary-layer meteorology*, 159, 193-220

967 Santamouris, M., Fiorito, F. 2021. On the impact of modified urban albedo on ambient temperature
968 and heat related mortality. *Solar Energy*, 216, 493-507

969 Schwaab, J., Meier, R., Mussetti, G., Seneviratne, S., Bürgi, C., Davin, E.L. 2021. The role of
970 urban trees in reducing land surface temperatures in European cities. *Nature Communications*,
971 12, 1-11

972 Scott, C.P., Beckley, M., Phan, M., Zawacki, E., Crosby, C., Nandigam, V., Arrowsmith, R. 2022.
973 Statewide USGS 3DEP Lidar Topographic Differencing Applied to Indiana, USA. *Remote*
974 *Sensing*, 14, 847

975 Seto, K.C., Güneralp, B., Hutyra, L.R. 2012. Global forecasts of urban expansion to 2030 and
976 direct impacts on biodiversity and carbon pools. *Proceedings of the National Academy of*
977 *Sciences*, 109, 16083-16088

978 Shen, P., Zhao, S., Ma, Y. 2021. Perturbation of urbanization to Earth's surface energy balance.
979 *Journal of Geophysical Research: Atmospheres*, 126, e2020JD033521

980 Shindell, D.T., Lamarque, J.-F., Schulz, M., Flanner, M., Jiao, C., Chin, M., Young, P., Lee, Y.H.,
981 Rotstayn, L., Mahowald, N. 2013. Radiative forcing in the ACCMIP historical and future
982 climate simulations. *Atmospheric Chemistry and Physics*, 13, 2939-2974

983 Shuai, Y., Masek, J.G., Gao, F., Schaaf, C.B. 2011. An algorithm for the retrieval of 30-m snow-
984 free albedo from Landsat surface reflectance and MODIS BRDF. *Remote Sensing of*
985 *Environment*, 115, 2204-2216

986 Shuai, Y., Masek, J.G., Gao, F., Schaaf, C.B., He, T. 2014. An approach for the long-term 30-m
987 land surface snow-free albedo retrieval from historic Landsat surface reflectance and
988 MODIS-based a priori anisotropy knowledge. *Remote Sensing of Environment*, 152, 467-
989 479

990 Stagakis, S., Chrysoulakis, N., Spyridakis, N., Feigenwinter, C., Vogt, R. 2019. Eddy Covariance
991 measurements and source partitioning of CO₂ emissions in an urban environment:
992 Application for Heraklion, Greece. *Atmospheric Environment*, 201, 278-292

993 Stokes, G.M., Schwartz, S.E. 1994. The Atmospheric Radiation Measurement (ARM) Program:
994 Programmatic background and design of the cloud and radiation test bed. *Bulletin of the*
995 *American Meteorological Society*, 75, 1201-1222

996 Sulla-Menashe, D., Friedl, M.A. 2018. User guide to collection 6 MODIS land cover (MCD12Q1
997 and MCD12C1) product. USGS: Reston, VA, USA, 1, 18

998 Sun, L., Chen, J., Li, Q., Huang, D. 2020. Dramatic uneven urbanization of large cities throughout
999 the world in recent decades. *Nature Communications*, 11, 1-9

1000 Tang, R., Zhao, X., Zhou, T., Jiang, B., Wu, D., Tang, B. 2018. Assessing the impacts of
1001 urbanization on albedo in Jing-Jin-Ji Region of China. *Remote Sensing*, 10, 1096

1002 Theil, H. 1950. A rank-invariant method of linear and polynomial regression analysis.
1003 *Indagationes Mathematicae*, 12, 173

-
- 1004 Theobald, D.M., Kennedy, C., Chen, B., Oakleaf, J., Baruch-Mordo, S., Kiesecker, J. 2020. Earth
1005 transformed: detailed mapping of global human modification from 1990 to 2017. *Earth*
1006 *System Science Data*, 12, 1953-1972
- 1007 Trlica, A., Hutyra, L., Schaaf, C., Erb, A., Wang, J. 2017. Albedo, land cover, and daytime surface
1008 temperature variation across an urbanized landscape. *Earth's Future*, 5, 1084-1101
- 1009 Velasco, E., Perrusquia, R., Jiménez, E., Hernández, F., Camacho, P., Rodríguez, S., Retama, A.,
1010 Molina, L. 2014. Sources and sinks of carbon dioxide in a neighborhood of Mexico City.
1011 *Atmospheric Environment*, 97, 226-238
- 1012 UNDESA (United Nations Department of Economic and Social Affairs). 2019. World Population
1013 Prospects 2019: Highlights. Available at:
1014 https://population.un.org/wpp/Publications/Files/WPP2019_Highlights.pdf.
- 1015 Wang, D., Liang, S., He, T., Yu, Y., Schaaf, C., Wang, Z. 2015. Estimating daily mean land surface
1016 albedo from MODIS data. *Journal of Geophysical Research: Atmospheres*, 120, 4825-4841
- 1017 Wang, X., Xiao, J., Li, X., Cheng, G., Ma, M., Zhu, G., Altaf Arain, M., Andrew Black, T., Jassal,
1018 R.S. 2019. No trends in spring and autumn phenology during the global warming hiatus.
1019 *Nature Communications*, 10, 1-10
- 1020 Wang, Z., Schaaf, C.B., Sun, Q., Shuai, Y., Román, M.O. 2018. Capturing rapid land surface
1021 dynamics with Collection V006 MODIS BRDF/NBAR/Albedo (MCD43) products. *Remote*
1022 *Sensing of Environment*, 207, 50-64
- 1023 Ward, H., Evans, J.G., Grimmond, C.S.B. 2013. Multi-season eddy covariance observations of
1024 energy, water and carbon fluxes over a suburban area in Swindon, UK. *Atmospheric*
1025 *Chemistry and Physics*, 13, 4645-4666
- 1026 Wong, N.H., Tan, C.L., Kolokotsa, D.D., Takebayashi, H. 2021. Greenery as a mitigation and
1027 adaptation strategy to urban heat. *Nature Reviews Earth & Environment*, 2, 166-181
- 1028 Wu, S., Wen, J., Gastellu-Etchegorry, J.-P., Liu, Q., You, D., Xiao, Q., Hao, D., Lin, X., Yin, T.
1029 2019. The definition of remotely sensed reflectance quantities suitable for rugged terrain.
1030 *Remote Sensing of Environment*, 225, 403-415
- 1031 Wu, S., Wen, J., Xiao, Q., Liu, Q., Hao, D., Lin, X., You, D. 2018. Derivation of Kernel functions
1032 for Kernel-driven reflectance model over sloping terrain. *IEEE Journal of Selected Topics in*
1033 *Applied Earth Observations and Remote Sensing*, 12, 396-409
- 1034 Wulder, M.A., Roy, D.P., Radeloff, V.C., Loveland, T.R., Anderson, M.C., Johnson, D.M., Healey,
1035 S., Zhu, Z., Scambos, T.A., Pahlevan, N. 2022. Fifty years of Landsat science and impacts.
1036 *Remote Sensing of Environment*, 280, 113195
- 1037 Xu, X., AzariJafari, H., Gregory, J., Norford, L., Kirchain, R. 2020. An integrated model for
1038 quantifying the impacts of pavement albedo and urban morphology on building energy
1039 demand. *Energy and Buildings*, 211, 109759
- 1040 Yang, C., Zhao, S. 2022. A building height dataset across China in 2017 estimated by the spatially-
1041 informed approach. *Scientific Data*, 9, 1-11
- 1042 Yang, X., Li, Y. 2015. The impact of building density and building height heterogeneity on average
1043 urban albedo and street surface temperature. *Building and environment*, 90, 146-156
- 1044 Zanaga, D., Van De Kerchove, R., De Keersmaecker, W., Souverijns, N., Brockmann, C., Quast,
1045 R., Wevers, J., Grosu, A., Paccini, A., Vergnaud, S. 2021. ESA WorldCover 10 m 2020 v100

1046 Zhang, H., Roy, D.P. 2016. Landsat 5 Thematic Mapper reflectance and NDVI 27-year time series
1047 inconsistencies due to satellite orbit change. *Remote Sensing of Environment*, 186, 217-2
1048 Zhang, Q., Seto, K.C. 2011. Mapping urbanization dynamics at regional and global scales using
1049 multi-temporal DMSP/OLS nighttime light data. *Remote Sensing of Environment*, 115, 2320-
1050 2329
1051 Zhang, W., Randall, M., Jensen, M.B., Brandt, M., Wang, Q., Fensholt, R. 2021. Socio-economic
1052 and climatic changes lead to contrasting global urban vegetation trends. *Global
1053 Environmental Change*, 71, 102385
1054 Zhou, Y., Li, X., Chen, W., Meng, L., Wu, Q., Gong, P., Seto, K.C. 2022. Satellite mapping of
1055 urban built-up heights reveals extreme infrastructure gaps and inequalities in the Global South.
1056 *Proceedings of the National Academy of Sciences*, 119, e2214813119
1057
1058
1059
1060
1061
1062
1063
1064
1065
1066
1067
1068
1069
1070
1071
1072
1073
1074
1075
1076
1077
1078
1079
1080
1081
1082
1083
1084
1085
1086
1087
1088

1089
1090

Table 1. Datasets used in this study by type.

Usage type	Dataset	Spatial extent	Resolution (m)	Frequency	Period	Purpose description	Reference
Surface reflectance	Landsat-5 SR	Global cities	30	16-day	1986-2011	Surface albedo & vegetation cover	Gorelick et al. 2017
	Landsat-7 SR	Global cities	30	16-day	2012-2013	Surface albedo & vegetation cover	Gorelick et al. 2017
	Landsat-8 SR	Global cities	30	16-day	2014-2020	Surface albedo & vegetation cover	Gorelick et al. 2017
Surface BRDF	MCD43A1	Global	500	Daily	2000-2020	BRDF database for LUT training	Gorelick et al. 2017; Wang et al. 2018
Surface albedo	Tower-based measurements	Table 2	-	10-30 min	Table 2	Albedo evaluation	Lipson et al. 2022a,b
	MCD43A3	Global	500	Daily	2000-2020	Albedo spatiotemporal analysis	Wang et al. 2018
Land cover type	ESA WorldCover	Global	10	Annual	2020	BRDF training sample selection	Zanaga et al. 2021
	MCD12Q1	Global	500	Annual	2001-2020	BRDF training sample selection	Gorelick et al. 2017; Wang et al. 2018
Solar radiation	BaRAD	Global	0.5° x 0.625°	Monthly	1980-2019	1) Diffuse skylight ratio estimate 2) Surface radiative forcing estimate	Chakraborty and Lee, 2021

1091
1092
1093
1094
1095
1096
1097
1098
1099
1100
1101
1102
1103
1104
1105
1106
1107
1108
1109
1110

1111
 1112
 1113
 1114
 1115
 1116

Table 2. Flux sites used for albedo evaluation, Tower height and impervious area fraction are available from Lipson et al.(2022a) and <https://mcr.unibas.ch/dev/sqlldb/index.php?nav=dbplot>. Footprint diameter (D) of tower measurement ($D = 2H \cdot \tan(\text{FOV}/2)$) is calculated from tower height (H) and sensor’s field of view (FOV) according to Román et al. 2009.

Site name	City	Country	Latitude (°)	Longitude (°)	Tower height (m)	Footprint diameter (m)	Impervious area fraction	Observation year (s)	Reference
Amsterdam	Amsterdam	The Netherlands	52.367	4.893	40	505	0.68	2019-2020	-
Baltimore	Baltimore	United States	39.413	-76.522	37	467	0.31	2002-2006	Crawford et al. 2011
Capitole	Toulouse	France	43.604	1.445	48	606	0.90	2004-2005	Goret et al. 2019
Escandon	Mexico	Mexico	19.404	-99.176	37	467	0.94	2011-2012	Velasco et al. 2014
Heckor	Heraklion	Greece	35.336	25.133	27	341	0.92	2019-2020	Stagakis et al. 2019
Jungnang	Seoul	South Korea	37.591	127.079	42	524	0.97	2017-2019	Hong et al. 2020
KingsCollege	London	United Kingdom	51.512	-0.117	50	631	0.79	2012-2013	Bjorkegren et al. 2015
Klingelbergstrasse	Basel	Switzerland	47.562	7.581	40	505	0.79	2003-2021	Feigenwinter et al. 2018
KlingelbstrStr.schlucht	Basel	Switzerland	47.561	7.581	2	25	0.79	2014-2020	Feigenwinter et al. 2018
Kumpula	Helsinki	Finland	60.203	24.961	31	391	0.46	2011-2021	Karsisto et al. 2016
Lipowa	Łódź	Poland	51.763	19.445	37	467	0.76	2008-2012	Fortuniak et al. 2013
Narutowicza	Łódź	Poland	51.773	19.481	42	530	0.65	2008-2012	Fortuniak et al. 2013
Ochang	Ochang	South Korea	36.720	127.434	19	240	0.47	2015-2017	Hong et al. 2020
Preston	Melbourne	Australia	-37.731	145.015	40	505	0.62	2003-2004	Coutts et al. 2007
Sunset	Vancouver	Canada	49.226	-123.078	24	303	0.68	2012-2016	Crawford and Christen, 2015
SurreyHills	Melbourne	Australia	-37.827	145.099	38	480	0.54	2004-2004	Coutts et al. 2007
Swindon	Swindon	United Kingdom	51.585	-1.798	13	158	0.49	2011-2013	Ward et al. 2013
TelokKurau	Singapore	Singapore	1.314	103.911	21	253	0.85	2006-2007	Roth et al. 2017
Torni	Helsinki	Finland	60.168	24.939	60	758	0.77	2011-2013	Järvi et al. 2018
WestPhoenix	Arizona	United States	33.484	-112.143	22	278	0.48	2011-2012	Chow, 2017
Yoyogi	Tokyo	Japan	35.665	139.685	52	657	0.92	2016-2020	Ishidoya et al. 2020

1117
 1118
 1119

Note: The KlingelbstrStr.schlucht site with a 2-m tower height observes the fluxes of grassland in urban environment.